http://dx.doi.org/10.1016/j.ijplas.2019.06.013


# A finite strain thermodynamically-based constitutive modeling and analysis of viscoelastic-viscoplastic deformation behavior of glassy polymers

J. Wang [a, b], L.F. Peng [a], Y.J. Deng [a], X.M. Lai [a, *], M.W. Fu [b, #], J. Ni [c]

[a] State Key Laboratory of Mechanical System and Vibration, Shanghai Jiao Tong University, Shanghai 200240, People's Republic of China

[b] Department of Mechanical Engineering, The Hong Kong Polytechnic University, Hung Hom, Kowloon, Hong Kong

[c] Department of Mechanical Engineering, University of Michigan, Ann Arbor, MI 48109, USA

[*, #] Corresponding author

E-mail addresses: xmlai@sjtu.edu.cn (X.M. Lai), mmmwfu@polyu.edu.hk (M.W. Fu)

## Abstract

In elastic and plastic deformation of glassy polymers and with the increase of deformation, the material would exhibit elastic, viscoelastic, and viscoelastic-viscoplastic (VE-VP) responses in sequence. These deformation behaviors should be constitutively modeled in such a way to accurately and efficiently simulate many important physical behaviors and phenomena involved in polymer deformation and processing. The elastic and viscoelastic deformation behavior in the pre-yield region can be well represented by the existing constitutive models. However, the VE-VP response in the post-yield region, such as

stress relaxation and strain recovery behaviors, cannot be well modeled yet. In this research, a series of uniaxial compression tests of the stress relaxation and the loading-unloading-recovery behaviors of glassy polymer were firstly carried out. The experimental phenomena show strain-rate-dependent characteristics that cannot be explained by the thermally-activated viscosity/viscoplasticity theory. Therefore, it is proposed that a glassy polymer can be treated as a glassy network linked by the secondary bonds and entanglements; while the glassy network is locally yielded and elastically distorted in the pre-yield region, giving rise to a glassy network resistance (GNR) which accounts for the strain-rate-dependent characteristics. A finite strain thermodynamically-based constitutive model was then proposed to incorporate the effects of the GNR. Finally, the newly proposed model was calibrated and its predictive capability was elaborated with the comparison of experiments as well as two widely reported models. The predicted results demonstrate that the GNR is critical in controlling the post-yield stress relaxation and strain recovery. In addition, the nonlinear evolution of the GNR plays a key role in controlling the nonlinear pre-peak hardening and the nonlinear unloading curve. This research thus not only provides a new constitutive theory for modeling of the VE-VP deformation behavior of glassy polymers, but also advances the understanding of the mechanical responses of glassy polymers in deformation process.

Keywords: Finite strain, Viscoelastic-viscoplastic, Yield, Stress relaxation, Strain recovery

## 1. Introduction

The deformation behavior of glassy polymers in the post-yield region is well-known to be of viscoelastic-viscoplastic (VE-VP) characteristics combining both glass-like and rubber-like responses (Bergstrom, 2015; Morelle, 2015). The widely reported constitutive behaviors include the strain-rate-dependent yield and flow (Farrokh and Khan, 2010), stress relaxation

(Liu et al., 2015), strain recovery at zero stress after unloading (Heinz et al., 2016), hysteresis loop in cyclic loading-unloading test (Krairi and Doghri, 2014), etc. To accurately and efficiently representing these behaviors by constitutive modeling is critical for investigation of a lot of physical phenomena in the processing of the polymers. The common applications include the imprinting (embossing) of micro/nanostructures on a polymer substrate (Jena et al., 2011), incremental forming of sheet polymer parts (Marques et al., 2012), impact perforation of polymer-metal laminates (Mohagheghian et al., 2016), and scratch process of polymer materials (Jiang et al., 2017), etc.

Research on modeling of the deformation behaviors of glassy polymers dates back to about five decades ago and was pioneered by Haward and Thackray (1968). Based on the far-reaching Haward-Thackray assumption which says that the material's total resistance to deformation can be additively decomposed into an intermolecular resistance (IR) and a rubbery network resistance (RNR), many three-dimensional (3D) constitutive models were developed for finite element analysis (FEA) applications. The widely-reported ones include the classical Boyce-Parks-Argon (BPA) model (Boyce et al., 1988a, b), the model of Buckley and Jones (1995), and the model of Govaert et al. (2000). These models can acceptably represent the overall stress-strain response during loading. They perform quite similarly in many aspects especially in describing the elasto-viscoplastic (EVP) response during loading and are usually called EVP models. However, they cannot model the realistic yield peak and unloading behavior and are not suitable for applications where strain rate or temperature varies with a wide range. Moreover, since these models overlook the viscoelastic response, they cannot accurately and correctly represent many important behaviors such as strain recovery at zero stress, stress relaxation, and so on. In the last two decades, a lot of researchers have endeavored to improve these models. Many advanced models were

developed due to the availability of more state-of-the-art simulation tools and measurement devices and the need to explore more unknown deformation behaviors in manufacturing and processing of glassy polymers.

The first majority of the researchers are more focused on accurately modeling of the EVP response, especially the yield, strain softening, and strain hardening behaviors. Buckley et al. (2004) further enhanced the Buckley-Jones model with a fictive temperature to represent the strain softening due to physical rejuvenation, giving rise to the so-called Oxford glass-rubber (OGR) model. Moreover, Govaert and coauthors (Klompen et al., 2005; Meijer and Govaert, 2005) introduced aging kinetics into their model to incorporate the effect of thermomechanical history on the yield strength, bringing about the so-called Eindhoven glassy polymer (EGP) model. To achieve accurate representation of the yield peak, Wu and Buckley (2004) and van Breemen et al. (2011) extended the OGR model and the EGP model, respectively, into multi-mode ones with a spectrum of stress-dependent relaxation times. The multi-mode ones, which are constructed under the parallel rheological framework (PRF) like the generalized Maxwell (GM) model, can also be used in simulating the viscoelastic response. Following the multi-mode approach, Xiao and Nguyen (2016) presented a thermodynamic approach for modeling of the strain softening based on the effective temperature theory (Xiao and Nguyen, 2015). To encompass a wide temperature and strain-rate range, Anand et al. (2009), Ames et al. (2009) and Srivastava et al. (2010) developed a thermo-mechanically coupled model, which will be termed as the Anand-Ames-Srivastava (AAS) model in this paper. With the introduction of an elasto-plastic back stress, the AAS model can acceptably simulating the unloading behavior at a large strain in contrast to many other models. In recent years, Bouvard et al. (2013) developed an internal state variable model for predicting the time, thermomechanical, and stress state dependence of glassy

polymers; Poulain et al. (2014) expanded the BPA model with modification of Argon's viscoplastic flow law to enable more accurate modeling of the temperature and strain-rate dependence; Garcia-Gonzalez et al. (2017) developed a hyperelastic-thermoviscoplastic model which pays special attention to thermal expansion and thermal softening resulted from the plastic-dissipation-induced self-heating; the works of Johnsen et al. (2019) and Li et al. (2019) also stressed on modeling of the self-heating; to incorporate the relaxation of molecular orientation and its effect on the strain hardening behavior, Garcia-Gonzalez et al. (2018) further added a viscoelastic mode into their model while Xiao and Tian (2019) proposed using a dissipative back-stress tensor.

The second majority of the researchers work on how to include the viscoelastic response coupled with the viscoplastic response for better modeling of the strain recovery, stress relaxation, loading-unloading hysteresis loop, etc. A model able to describe both the viscoelastic and viscoplastic responses can be termed as a VE-VP model. A popular approach to develop such a model is to decompose the total deformation into viscoelastic and viscoplastic parts, which leads to a stress coupling between the viscoelastic and viscoplastic responses (such a model may be further termed as a stress-coupled VE-VP model). Khan and Zhang (2001) assumed that the viscoplastic flow is driven by the viscoelastic stress represented by a Zener-like model in Maxwell representation. Holopainen and coauthors (Holopainen, 2013; Holopainen and Barriere, 2018; Holopainen et al., 2017) extended the BPA model by replacing the Hookean spring with a Zener-like model in Kelvin representation. Doghri and coauthors (Gudimetla and Doghri, 2017; Krairi and Doghri, 2014; Krairi et al., 2019; Miled et al., 2011) adopted the GM model for the viscoelastic part and developed a series of constitutive theories, with consideration of the finite strain, thermo-mechanical coupling and damage; the model of Nguyen et al. (2016) or Zerbe et al. (2017) is

constructed similarly but with different description of the damage. Yu and coauthors (Yu et al., 2017a; Yu et al., 2017b; Yu et al., 2016) constructed the viscoelastic part based on Schapery's nonlinear viscoelastic model and proposed a series of constitutive theories aimed at modeling the cyclic deformation. In addition, Anand and Ames (2006) developed a model by extending the generalized Kelvin-Voigt model to the finite deformation range, presenting an alternative way for formulating a stress-coupled VE-VP model.

Another practical approach to incorporate the viscoelastic response is to introduce multiple relaxation modes into the EVP models under the PRF as has been demonstrated by the multi-mode OGR and EGP models, the model of Garcia-Gonzalez et al. (2018), etc. A multi-mode EVP model couples the viscoelastic and viscoplastic responses with strain and thus may be termed as a strain-coupled VE-VP model. Within the finite deformation theory, it is a challenge to choose a viscoelastic strain measure for a stress-coupled VE-VP model (Gudimetla and Doghri, 2017), while the strain-coupled models naturally avoid this challenge. One more advantage of the strain-coupled models is that they are ready for incorporating different relaxation mechanisms. For instance, Mathiesen et al. (2014) employed a Rolie-Poly viscoelastic mode to simulate the melt-stage stress relaxation of a polymer near the glass transition temperature (Tg); Qi et al. (2019) developed a model consisting of a elastic-plastic mode and mutiple viscoelatic modes for precisely simulating the stress-strain response in cyclic loading. In addition, the viscoplasticity theory based on overstress (VBO), which represents the VE-VP deformation behavior in a unified way (Colak, 2005; Khan and Yeakle, 2011), is quite worth noting; Ayoub et al. (2010) developed a multi-mode model which adopts the VBO to represent the IR and shows significantly improved predictive capability for the unloading and stress relaxation behaviors at large deformation. The VE-VP model of Drozdov and coauthors (Drozdov and Christiansen, 2008;

Drozdov and Gupta, 2003), which is based on the transient network theory, is also very interesting.

From the above review, it can be concluded that a considerable progress has been made in constitutive modeling of the deformation behaviors of glassy polymers. Nevertheless, due to a lack of in-depth understanding of the molecular origin of stress in the deformation of glassy polymers, the post-yield strain recovery and stress relaxation behaviors cannot be well represented yet. It should be noted that since the strain recovery can provide information on the deformation state while the stress relaxation is associated with the molecular mobility and the relaxation time directly represents the "material clock" (Kim et al., 2013; Lee et al., 2010), a model which can correctly capture these two behaviors is of a great importance in predicting many other constitutive behaviors. When a glassy polymer is stretched, both the interchain and intrachain stresses will arise and there is an intricate coupling between the two stresses (Cheng and Wang, 2013). Due to the formation of chain entanglements, it is widely accepted that a rubbery network is formed and embedded in the glassy polymer. A convenient and effective way to model such a molecular picture is to employ the Haward-Thackray assumption; the coupling between the interchain and intrachain stresses, however, is much more complicated. It is recently confirmed by Li et al. (2018) that the stress in the post-yield deformation of glassy polymers should contain a high level of intrachain part. Moreover, the relaxation rate of this intrachain stress is governed by the deformation rate (Bending et al., 2014; Kim et al., 2013; Liu et al., 2015). Obviously, this intrachain stress is distinct from the one represented by the RNR. According to the experimental investigation of this research, this intrachain stress can be rationalized by the elastic distortion of a glassy network linked by the secondary bonds and entanglements. For clarity, it is termed as a glassy network stress/resistance (GNR). The GNR plays essential roles in controlling the VE-

VP deformation behavior but is not considered by the existing constitutive models. Thus, to incorporate it into the total deformation resistance, a new physically-based and thermodynamically-based constitutive model was proposed in this research. The new model was validated by corroboration with experiments. In contrast to the existing models, the new model can concurrently represent the stress relaxation and loading-unloading-recovery behaviors in the post-yield region, demonstrating a largely improved accuracy and capability for modeling of the VE-VP deformation behavior of glassy polymers.

## 2. Experimental phenomena

For a better understanding of the VE-VP deformation behavior of glassy polymers as well as how the GNR affects it, the uniaxial compression tests for study of the stress relaxation and loading-unloading-recovery behaviors were conducted with a commercially available bisphenol-A polycarbonate (PC) glass (Tg $\approx$ 145 ℃). The PC glass was machined into the cylindrical specimens with the diameter of 5 mm and the height of 5 mm. The specimens were annealed by heating to 10 ℃ above the Tg, holding for about two hours and cooling to a room temperature of about 23 ℃ slowly. All the tests were then done by a material testing system (MTS, Instron ElectroPuls E10000) at the room temperature. In addition, a grease lubricant was applied between the specimen and the compression plate to reduce friction and avoid an obvious barreling.

### 2.1. Stress relaxation behavior

The stress relaxation behavior of glassy polymers depends on both the strain and strain rate, which has been experimentally investigated by several researchers (Kim et al., 2013; Lee et al., 2010; Li et al., 2018; Liu, 2015). It was reported that the post-yield stress relaxation is only slightly affected by the strain levels but dominated by the strain rate. In this

study, stress relaxation tests with variation of strain or strain rate were conducted to check the reported phenomena, illustrate the key features of the GNR, and provide data for the constitutive modeling. The stress relaxation behavior of the PC glass was tested by measuring the stress response after loading with a constant engineering strain rate to a specified strain. The stress relaxation process was measured up to 1800 s so that the additional stress that might be further relaxed (in a practical measurement period) could be neglected. The stress applied after the loading, the current stress at a relaxation time of $t$, and the stress at the end of the measurement are denoted as $\sigma_0$, $\sigma_t$, and $\sigma_{inf}$, respectively. $\sigma_{inf}$ is approximately equal to the final equilibrium stress at the given strain. The total relaxed stress, denoted as $\sigma_r$, can be calculated as $\sigma_r = \sigma_0 - \sigma_{inf}$.

Fig. 1 shows the stress relaxation results obtained from the set of tests with variation of strain. The strain rate for the loading is $1\times10^{-3}$ $s^{-1}$. In Fig. 1a, the solid lines are the stress-strain curves and the dashed line is $\sigma_r$ plotted as a function of the strain. With the increase of the strain, $\sigma_r$ continues to increase. The increase of $\sigma_r$ is quite significant around the yield peak but becomes insignificant at larger strains. The corresponding stress relaxation curves presented in Fig. 1b demonstrate that the stress relaxation rate is also increased with the increased strain and varies in a similar way as that of $\sigma_r$. The strain dependence indicates that the molecular mobility of the glassy polymer is increased significantly during the yielding process but cannot be substantially increased anymore in the post-yield region. If the post-yield variation is neglected, the strain dependence may be explained by the thermally-activated viscosity/viscoplasticity theory, for instance, the widely used Eyring's or Argon's viscoplastic flow law, which assumes stress/strain-dependent relaxation times of the material. However, it should be noted that the strain dependence of stress relaxation in the

strain softening region is still obvious.

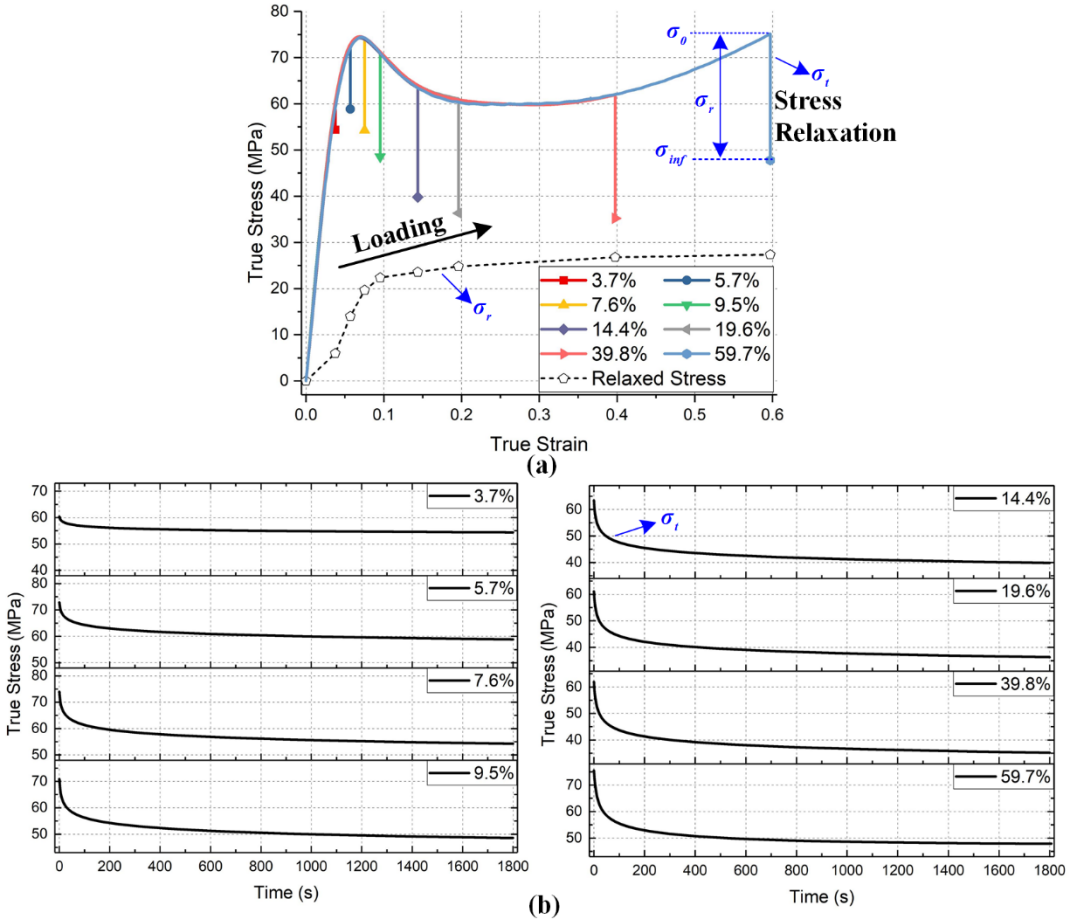


**Fig. 1.** Stress relaxation of the PC glass after loading to different strains with a constant strain rate of $1\times10^{-3}$ $s^{-1}$: (a) stress-strain curves and (b) the corresponding stress relaxation curves. The dashed line in (a) is the total relaxed stress plotted as a function of strain.

Fig. 2 shows the stress relaxation results obtained from the set of tests with variation of strain rate. A post-yield strain of about 60% was applied for the tests; the strain rates were varied in the range of $1\times10^{-4}$ to $1\times10^{-1}$ $s^{-1}$. According to Eyring's or Argon's viscoplastic flow law, $\sigma_{inf}$ represents the flow stress in the case of a nearly zero strain rate, while $\sigma_r$ represents the increased viscous stress due to the increased strain rate. Thus, $\sigma_{inf}$ should be rate-independent, namely, relaxation of the IR represented by the thermally-activated

viscosity model should approximately lead to a same value of $\sigma_{inf}$. Nevertheless, as shown by Fig. 2a, $\sigma_{inf}$ is decreased significantly with the increasing strain rate. The self-heating due to the viscous dissipation may explain the decrease of $\sigma_{inf}$ for the cases with the high strain rates (in the range of $1\times10^{-2}$ to $1\times10^{-1}$ $s^{-1}$), but not for those with slower strain rates. Moreover, the relaxation curves reveal that the stress relaxation rate is also dominated by the strain rate. Since the RNR cannot be relaxed in such a short measurement time, the strain-rate dependence can only be rationalized by the relaxation of the GNR. In other words, the GNR can be treated as a viscoelastic stress with a relaxation rate dictated by the prior deformation rate.

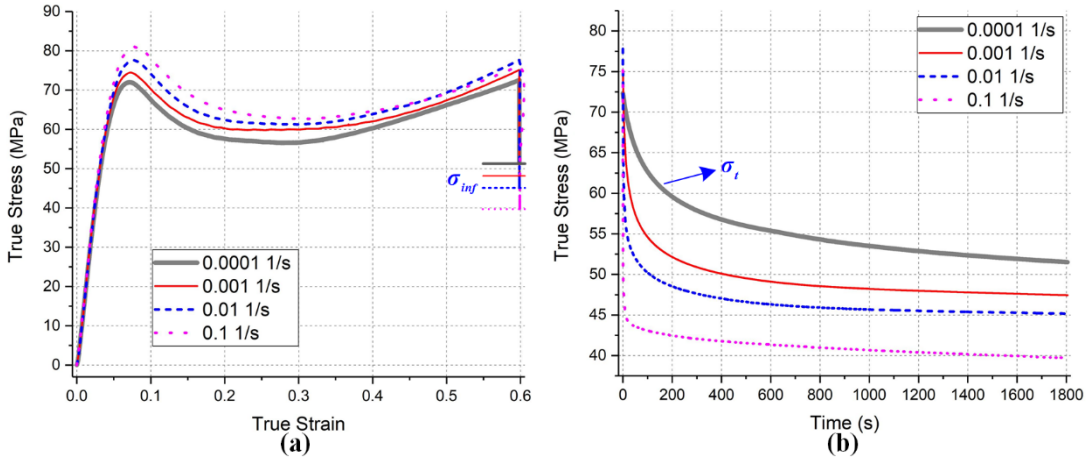


**Fig. 2.** Strain-rate-dependent stress relaxation of the PC glass: (a) stress-strain curves and (b) the corresponding stress relaxation curves.

## 2.2. Loading-unloading-recovery behavior

To explore the VE-VP deformation behavior and how the GNR would affect it, the loading-unloading-recovery tests were conducted with a variety of strains and strain rates. The stress-strain curves during loading and unloading were measured with a constant engineering strain rate. The strain-time curves after unloading, namely, the strain recovery at zero stress, were measured by a force-controlled step. In addition, a measurement time of

1200 s was chosen so that the additional strain which might be further recovered (in a practical measurement period) could be neglected. Fig. 3 shows the experimental results at a strain rate of $1\times10^{-3}$ $s^{-1}$ and an applied strain of 99.5%. The loading curve was characterized by the initial linear stiffness, nonlinear pre-peak hardening, yielding, strain softening and strain hardening. The unloading curve is nonlinear, and its stiffness is gradually decreased as the strain recovers. The total recovered strain is about 25% of the applied strain. The strain recovered at zero stress is about 4% of the applied strain and about 17% of the total recovered strain. Therefore, to accurately predict the residual strain, it is quite necessary for a constitutive model to represent the strain recovery behavior during unloading as well as at zero stress. In the following paper, the residual strain, the total recovered strain, and the strain recovered at zero stress are denoted as $\varepsilon_{res}$, $\varepsilon_{rec}$ and $\varepsilon_{zer}$, respectively.

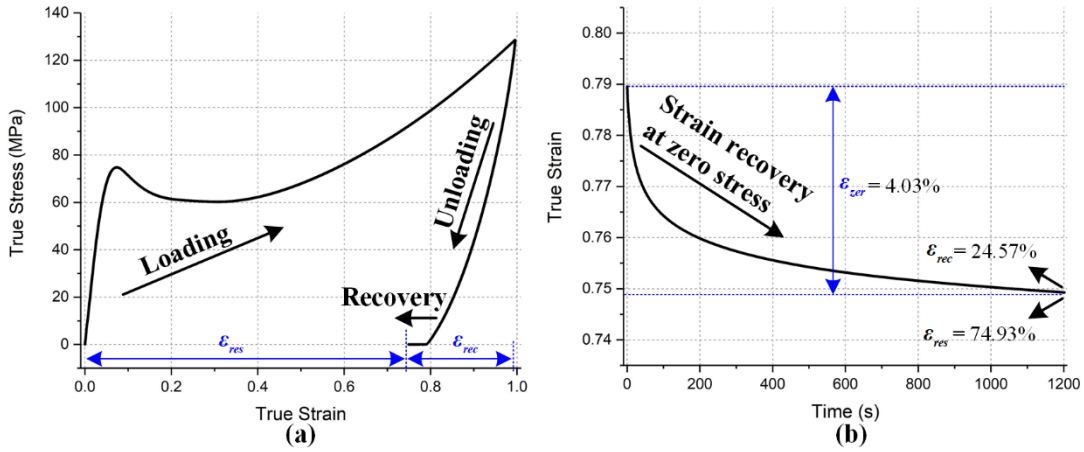


**Fig. 3.** Loading-unloading-recovery behavior of the PC glass: (a) stress-strain curve, and (b) strain recovery at zero stress.

Before discussion of the post-yield deformation, a set of tests with different strains in the pre-peak region were conducted for analyzing the yielding process and the origination of the GNR. The strain rate employed was $1\times10^{-3}$ $s^{-1}$. The results are presented in Fig. 4. In the nearly-linear part of the stress-strain curve, the applied strain is totally recoverable during

unloading. With increasing the strain to the nonlinear pre-peak hardening region, the energy dissipation observed in a deformation cycle is increased significantly. The glassy polymer is deformed as a viscoelastic body. As a result, the strain cannot totally recover during unloading anymore. However, due to the increased $\varepsilon_{zer}$, $\varepsilon_{res}$ is still negligible. Thus, the yielding of the glassy polymer is a process that starts locally and then spreads to other unyielded part, while the unyielded part must be elastically distorted.

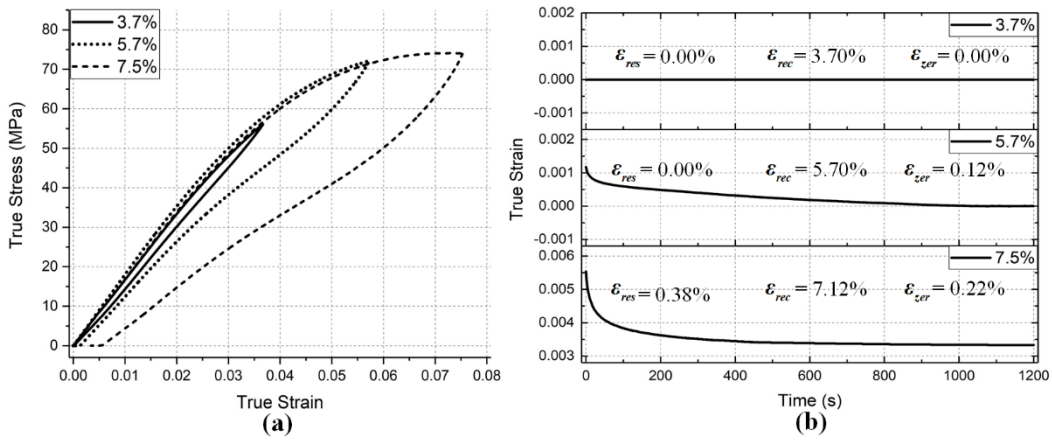


**Fig. 4.** Loading-unloading-recovery behavior of the PC glass in the pre-yield region: (a) stress-strain curves, and (b) the corresponding strain recovery at zero stress.

For further analysis, a physical interpretation of the yielding process is illustrated in Fig. 5. The glassy polymer is assumed to be composed of entangled and non-entangled chains (polymers composed of crystalline structures or only consisting non-entangled short chains are not considered in this research). The non-entangled chains reinforce the entangled chain network through the secondary bonds and a glassy network is formed. Before being dissociated, a secondary bond would work the same as an entanglement formed by the physical cross-link of the molecular chains, which supports the concept of the glassy network. When macroscopic deformation is applied, the glassy network first responds as an elastic body due to the large number of the secondary bonds. However, with the increasing

deformation, dissociation of the secondary bonds may take place at some local regions. A chain or a part of a chain in these regions, which is represented by the dashed line, is of higher mobility and would start its conformational changes first. Thus, the glassy network is locally yielded. The resistance to the local yielding is termed as a local-yielding resistance (LYR) in this paper. The LYR is a viscous stress as it is intermolecular friction in nature. At the same time, the unyielded part which contains the locally-yielded regions is elastically distorted. Thus, the glassy network is transformed from an elastic body to a viscoelastic one. With further increased deformation, the yielded regions would expand to major part of the glassy network and the glassy network is torn to pieces embedded in the yielded regions, leading to the macroscopic yielding and the start of the so-called viscoplastic flow. In the above analysis, it should be noted that the elastic distortion of the glassy network is associated with the deformation of the yielded regions. Therefore, the elastic distortion must contribute a part to the pre-yield hardening and thus rationalizes the origination of the GNR. Moreover, the macroscopic yield strength should contain both the LYR and the GNR.

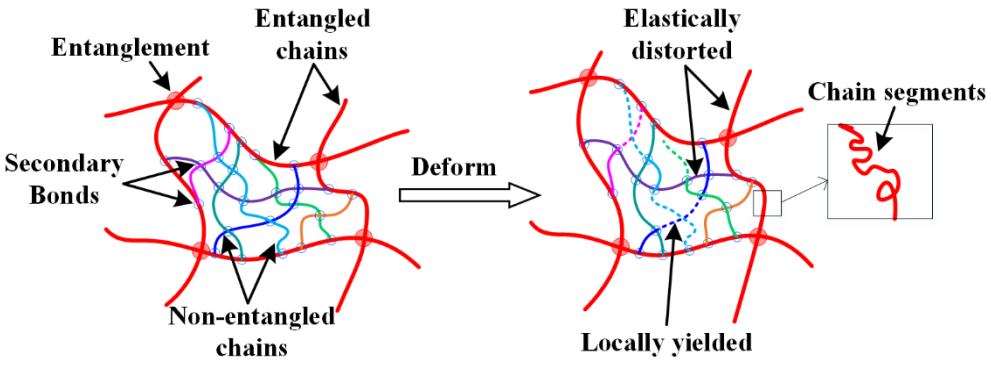


**Fig. 5.** Illustration of the formation of a glassy network and its yielding process

Fig. 6 and Fig. 7 display the loading-unloading-recovery behavior in the post-yield region as well as its strain-rate dependence. The strain rates tested were in the range of $1\times10^{-4}$ to $1\times10^{-1}$ $s^{-1}$. In addition to the viscoplastic loading behavior characterized by the strain-rate

dependent yield and flow, the results show that, the strain recovery at zero stress also depends on the strain rate significantly. With a higher strain rate, the strain recovery at zero stress will proceed faster. This strain-rate dependence is only slightly affected by the variation of the applied strain, although increasing the strain from about 10% to about 100% should induce a largely increased retractive intrachain stress in the rubbery network. Considering the key features of the GNR, it can be concluded that the rate of the strain recovery at zero stress is dominated by the relaxation of the GNR. In addition, the GNR must play a role in controlling the unloading behavior.

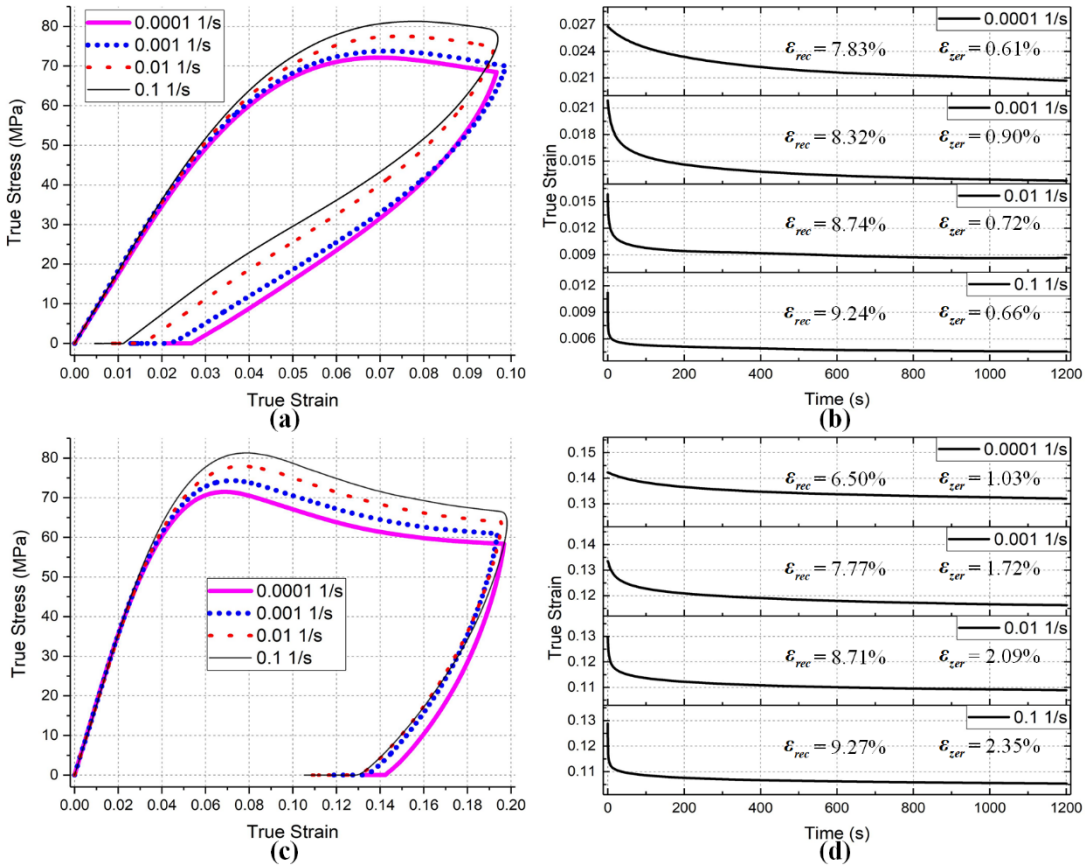


**Fig. 6.** Loading-unloading-recovery behavior of the PC galss in the strain-softening region and its rate dpendence: (a) and (c) are stress-strain curves, while (b) and (d) are the corresponding strain-recovery curves at zero stress.

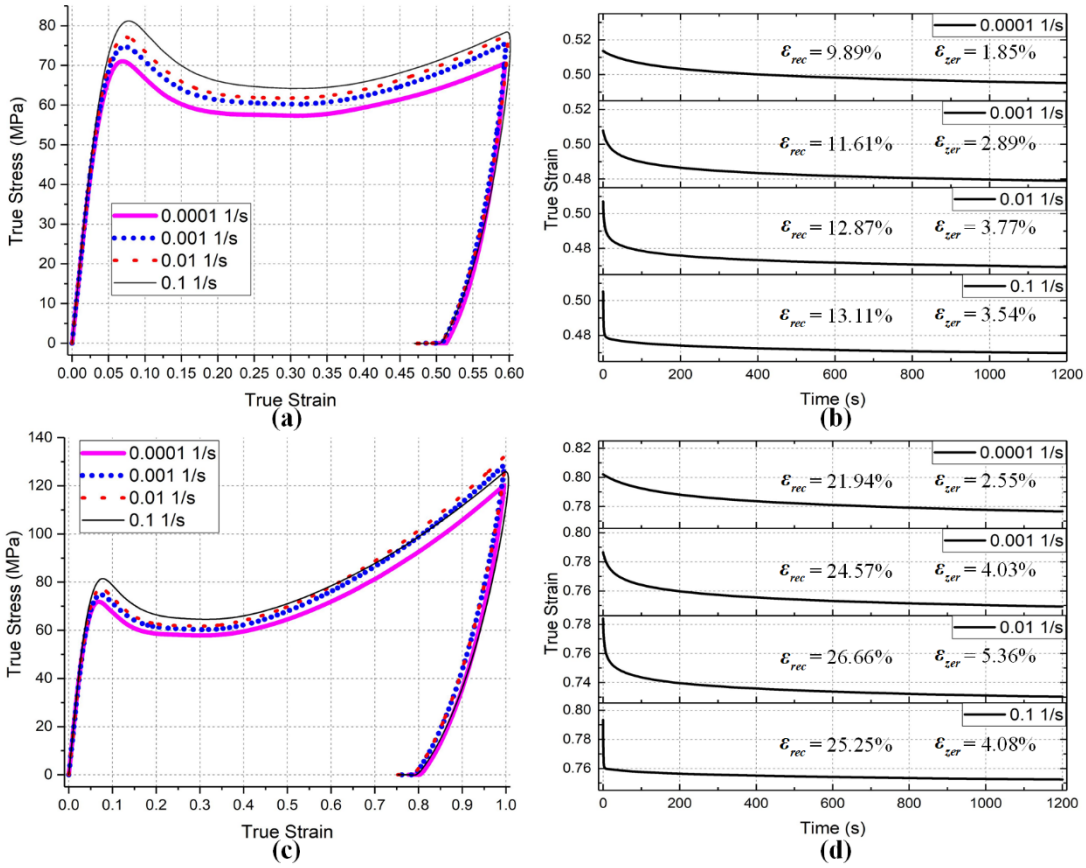


**Fig. 7.** Loading-unloading-recovery behavior of the PC galss in the strain-hardening region and its strain-rate dependence: (a) and (c) are stress-strain curves, while (b) and (d) are the corresponding strain-recovery curves at zero stress.

## 3. Description of the constitutive model

### 3.1. Decomposition of the deformation resistance

Fig. 8 illustrates the rheological framework for the present model. Firstly, following the Haward-Thackray assumption, the deformation resistance is also additively separated into the IR and the RNR. The RNR corresponds to the intrachain stress due to the conformational entropy and the limited extensibility of the molecular chains; it is represented by the spring element S0. The IR is much more complicated than the RNR due to the hierarchical structure of the glassy network. For accurate and efficient modeling of the strain recovery behavior, it is assumed that the IR can be additively decomposed into two parts representing the different

contributions from the deformation of the entangled and non-entangled chains. The elasticity of the glassy network before the start of the local yielding depends on the stiffness of the secondary bonds as well as the molecular chains, so it can be represented by the spring elements S1 and S2. The local yielding corresponds to the dissociation of the secondary bonds and the subsequent conformational changes. The LYR is viscous and is represented by the dashpot elements (D1 and D2 for the entangled and non-entangled chains, respectively). Furthermore, based on the physical interpretation of the macroscopic yielding, the GNR can be represented by the polymer elements (P1 and P2 for the entangled and non-entangled chains, respectively) in parallel connection with the dashpot elements. The polymer elements are introduced to represent the deformation of the glassy network associated with the deformation of the locally-yielded regions.

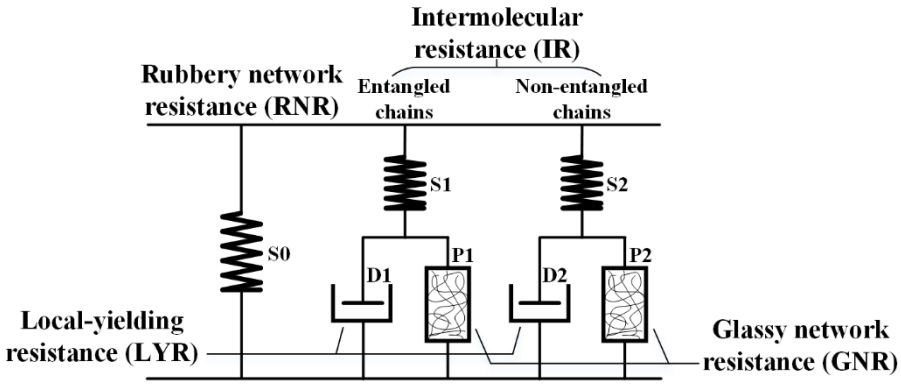


**Fig. 8.** Rheological framework of the constitutive model

3.2. Kinematics

The motion of a continuum body can be described by the following mapping:

$$\mathbf{x} = \chi(\mathbf{X}, t) \tag{1}$$

where $\mathbf{X}$ and $\mathbf{x}$ are the material points in the reference configuration $\Omega_0$ and the current configuration $\Omega$, respectively. The deformation gradient tensor $\mathbf{F}$ is defined as

$$\mathbf{F} = \frac{\partial \chi(\mathbf{X}, t)}{\partial \mathbf{X}} \tag{2}$$

The volume change of the continuum body can be represented by the determinant of $\mathbf{F}$

$$J = \det(\mathbf{F}) > 0 \tag{3}$$

In accordance with the decomposition of the deformation resistance, the non-entangled chains are assumed to deform in parallel with the entangled chains, namely

$$\mathbf{F} = \mathbf{F}_1 = \mathbf{F}_2 \tag{4}$$

where the subscripts 1 and 2 denote the entangled and non-entangled chains, respectively. In the following paper, the subscript 1 or 2 will be substituted by $I$ where the description is the same for both.

To model the VE-VP deformation behavior of the glassy network, $\mathbf{F}_I$ is multiplicatively decomposed into an elastic part $\mathbf{F}_I^e$ and an inelastic part $\mathbf{F}_I^i$:

$$\mathbf{F}_I = \mathbf{F}_I^e \mathbf{F}_I^i \tag{5}$$

Furthermore, it is assumed that the inelastic deformation/flow is incompressible, namely,

$$J_I^i = \det(\mathbf{F}_I^i) = 1 \tag{6}$$

Thus

$$J_I^e = \det(\mathbf{F}_I^e) = J \tag{7}$$

With Eq. (5) the velocity gradient $\mathbf{L}_I$ in $\Omega$ can also be additively decomposed into an elastic part $\mathbf{L}_I^e$ and an inelastic part $\mathbf{L}_I^i$:

$$\mathbf{L}_I = \dot{\mathbf{F}}_I \mathbf{F}_I^{-1} = \mathbf{L}_I^e + \mathbf{L}_I^i \tag{8}$$

where $\mathbf{L}_I^e = \dot{\mathbf{F}}_I^e \mathbf{F}_I^{e-1}$ and $\mathbf{L}_I^i = \mathbf{F}_I^e \bar{\mathbf{L}}_I^i \mathbf{F}_I^{e-1}$. $\bar{\mathbf{L}}_I^i = \dot{\mathbf{F}}_I^i \mathbf{F}_I^{i-1}$ is the inelastic velocity gradient

defined in the elastic intermediate configuration $\bar{\Omega}$.

As is standard, the inelastic deformation rate $\bar{\mathbf{D}}_I^i$ and spin rate $\bar{\mathbf{W}}_I^i$ in $\bar{\Omega}$ are given as the symmetric and skew parts of $\bar{\mathbf{L}}_I^i$, respectively:

$$\bar{\mathbf{D}}_I^i = \mathrm{sym}\bar{\mathbf{L}}_I^i = \frac{1}{2}\left(\bar{\mathbf{L}}_I^i + \bar{\mathbf{L}}_I^{i\mathrm{T}}\right) \tag{9}$$

$$\bar{\mathbf{W}}_I^i = \mathrm{skw}\bar{\mathbf{L}}_I^i = \frac{1}{2}\left(\bar{\mathbf{L}}_I^i + \bar{\mathbf{L}}_I^{i\mathrm{T}}\right) \tag{10}$$

Assume the inelastic spin rate $\bar{\mathbf{W}}_I^i = 0$, then

$$\bar{\mathbf{L}}_I^i = \bar{\mathbf{D}}_I^i \tag{11}$$

The evolution equation for $\mathbf{F}_I^i$ can be expressed as

$$\dot{\mathbf{F}}_I^i = \bar{\mathbf{L}}_I^i \mathbf{F}_I^i = \bar{\mathbf{D}}_I^i \mathbf{F}_I^i \tag{12}$$

Finally, the right and left polar decompositions of $\mathbf{F}$ are given by

$$\mathbf{F} = \mathbf{RU} = \mathbf{VR} \tag{13}$$

where $\mathbf{R}$ is the rotation tensor; $\mathbf{U}$ and $\mathbf{V}$ are the right and left stretching tensors. Then, the right and left Cauchy-Green tensors are defined as

$$\mathbf{C} = \mathbf{F}^{\mathrm{T}}\mathbf{F} = \mathbf{U}^2, \ \mathbf{B} = \mathbf{F}\mathbf{F}^{\mathrm{T}} = \mathbf{V}^2 \tag{14}$$

Similarly, the following Cauchy-Green tensors also can be defined:

$$\bar{\mathbf{C}}_I^e = \mathbf{F}_I^{e\mathrm{T}}\mathbf{F}_I^e = \bar{\mathbf{U}}_I^{e2}, \ \mathbf{B}_I^e = \mathbf{F}_I^e\mathbf{F}_I^{e\mathrm{T}} = \mathbf{V}_I^{e2} \tag{15}$$

3.3. Thermodynamics

Let $\psi$ denotes the Helmholtz free energy and $P$ denotes the stress power per unit volume of $\Omega_0$, the Clausius-Duhem inequality in isothermal conditions can be expressed as

$$P-\dot{\psi}\geq 0 \tag{16}$$

As illustrated by the rheological scheme, $\psi$ is assumed to be additively decomposed into five parts:

$$\psi=\hat{\psi}_1^e\left(\bar{\mathbf{C}}_1^e\right)+\hat{\psi}_2^e\left(\bar{\mathbf{C}}_2^e\right)+\hat{\psi}_1^a\left(\bar{\mathbf{A}}_1\right)+\hat{\psi}_2^a\left(\bar{\mathbf{A}}_1\right)+\hat{\psi}_0\left(\mathbf{C}\right) \tag{17}$$

where $\hat{\psi}_1^e\left(\bar{\mathbf{C}}_1^e\right)$, $\hat{\psi}_2^e\left(\bar{\mathbf{C}}_2^e\right)$, $\hat{\psi}_1^a\left(\bar{\mathbf{A}}_1\right)$, $\hat{\psi}_2^a\left(\bar{\mathbf{A}}_2\right)$ and $\hat{\psi}_0\left(\mathbf{C}\right)$ are isotropic functions of $\bar{\mathbf{C}}_1^e$, $\bar{\mathbf{C}}_2^e$, $\bar{\mathbf{A}}_1$, $\bar{\mathbf{A}}_2$ and $\mathbf{C}$ respectively. The tensor $\bar{\mathbf{A}}_I$ is defined in $\bar{\Omega}$ and can be regarded as a conformation tensor which measures the elastic distortion of the glassy network coupled with the inelastic deformation while $\hat{\psi}_I^a\left(\bar{\mathbf{A}}_I\right)$ is an energy associated with this distortion and describes the GNR. $\hat{\psi}_0\left(\mathbf{C}\right)$ describes the RNR due to the conformational entropy and the limited extensibility of molecular chains. $\hat{\psi}_I^e\left(\bar{\mathbf{C}}_I^e\right)$ is used to model the initial stiffness due to the bond stretching.

The material time derivative of the free energy is

$$\dot{\psi}=\frac{\partial\hat{\psi}_1^e}{\partial\bar{\mathbf{C}}_1^e}:\dot{\bar{\mathbf{C}}}_1^e+\frac{\partial\hat{\psi}_2^e}{\partial\bar{\mathbf{C}}_2^e}:\dot{\bar{\mathbf{C}}}_2^e+\frac{\partial\hat{\psi}_1^a}{\partial\bar{\mathbf{A}}_1}:\dot{\bar{\mathbf{A}}}_1+\frac{\partial\hat{\psi}_2^a}{\partial\bar{\mathbf{A}}_2}:\dot{\bar{\mathbf{A}}}_2+\frac{\partial\hat{\psi}_0}{\partial\mathbf{C}}:\dot{\mathbf{C}} \tag{18}$$

where $\dot{\bar{\mathbf{A}}}_I$ represents the dynamics of $\bar{\mathbf{A}}_I$ and should be further prescribed by a constitutive model. Referring to the literature, two types of models may be adopted for $\dot{\bar{\mathbf{A}}}_I$: the kinematic hardening models for the polymer-viscoplasticity (Anand et al., 2009) and the tube models for the rheology of entangled polymer melts or solutions (Varchanis et al., 2018). In fact, both the two types of models can be expressed by the following equation:

$$\dot{\bar{\mathbf{A}}}_I=\bar{\mathbf{L}}_I^i\bar{\mathbf{A}}_I+\bar{\mathbf{A}}_I\bar{\mathbf{L}}_I^i-\mathbf{f}_I\left(\Lambda_I\right) \tag{19}$$

where the term $\bar{\mathbf{L}}_I^i\bar{\mathbf{A}}_I+\bar{\mathbf{A}}_I\bar{\mathbf{L}}_I^i$ describes the driving of $\bar{\mathbf{A}}_I$ away from its equilibrium by the

inelastic deformation, while the term $\mathbf{f}_I\left(\boldsymbol{\Lambda}_I\right)$ accounts for the recovery of $\bar{\mathbf{A}}_I$ back to its equilibrium. $\mathbf{f}_I\left(\boldsymbol{\Lambda}_I\right)$ is a tensor-valued function of a list of state variables denoted by $\boldsymbol{\Lambda}_I$ and defines the relaxation rate of the distorted glassy network. Since the glassy network is connected through the secondary bonds, with the increase of the distortion, the secondary bonds in the glassy network will be dissociated and the distortion can be relaxed. Moreover, since the distorted glassy network is coupled with (surrounded by or embedded in) the yielded regions, the higher molecular mobility of the yielded regions would lead to the distorted glassy network to be less constrained and be able to relax faster. Hence, $\mathbf{f}_I\left(\boldsymbol{\Lambda}_I\right)$ should be determined by both the distortion of the glassy network and the molecular mobility of the yielded regions. In addition, the strain and strain-rate dependence of stress relaxation may be explained by the molecular mobility of the yielded regions which is strain- and strain-rate dependent.

Assume $\bar{\mathbf{A}}_I$ to be symmetric, and since $\bar{\mathbf{L}}^i=\bar{\mathbf{D}}^i$ and $\hat{\psi}^a\left(\bar{\mathbf{A}}_I\right)$ is an isotropic function of $\bar{\mathbf{A}}_I$, Eq. (18) becomes

$$\begin{aligned}\dot{\psi}=&\frac{\partial\hat{\psi}_1^e}{\partial\bar{\mathbf{C}}_1^e}:\dot{\bar{\mathbf{C}}}_1^e+\frac{\partial\hat{\psi}_2^e}{\partial\bar{\mathbf{C}}_2^e}:\dot{\bar{\mathbf{C}}}_2^e+2\frac{\partial\hat{\psi}_1^a}{\partial\bar{\mathbf{A}}_1}\dot{\bar{\mathbf{A}}}_1:\bar{\mathbf{D}}_1^i-\frac{\partial\hat{\psi}_1^a}{\partial\bar{\mathbf{A}}_1}:\mathbf{f}_1\left(\boldsymbol{\Lambda}_1\right)\\&+2\frac{\partial\hat{\psi}_2^a}{\partial\bar{\mathbf{A}}_2}\dot{\bar{\mathbf{A}}}_2:\bar{\mathbf{D}}_2^i-\frac{\partial\hat{\psi}_2^a}{\partial\bar{\mathbf{A}}_2}:\mathbf{f}_2\left(\boldsymbol{\Lambda}_2\right)+\frac{\partial\hat{\psi}_0}{\partial\mathbf{C}}:\dot{\mathbf{C}}\end{aligned}\tag{20}$$

The stress power $P$ can be expressed as:

$$P=J\boldsymbol{\sigma}:\mathbf{L}=\boldsymbol{\tau}:\mathbf{L}=\mathbf{S}:\frac{1}{2}\dot{\mathbf{C}}\tag{21}$$

where $\boldsymbol{\sigma}$ is the total Cauchy stress, $\boldsymbol{\tau}=J\boldsymbol{\sigma}$ is the total Kirchhoff stress, and $\mathbf{S}=J\mathbf{F}^{-1}\boldsymbol{\sigma}\mathbf{F}^{-\mathrm{T}}=\mathbf{F}^{-1}\boldsymbol{\tau}\mathbf{F}^{-\mathrm{T}}$ is the total second Piola-Kirchhoff (P-K) stress. In line with the

decomposition of the deformation resistance, $\boldsymbol{\tau}$ is additively split into three parts:

$$\boldsymbol{\tau} = \boldsymbol{\tau}_1 + \boldsymbol{\tau}_2 + \boldsymbol{\tau}_0 \tag{22}$$

where $\boldsymbol{\tau}_1$ and $\boldsymbol{\tau}_2$ represent the IRs originated from the entangled and non-entangled chains, respectively, and $\boldsymbol{\tau}_0$ represents the RNR. Correspondingly, $P$ is also split into three parts:

$$P = P_1 + P_2 + P_0 \tag{23}$$

where $P_1 = \boldsymbol{\tau}_1 : \mathbf{L}$, $P_2 = \boldsymbol{\tau}_2 : \mathbf{L}$ and $P_0 = \boldsymbol{\tau}_0 : \mathbf{L}$. The stress power $P_0$ can be expressed as

$$P_0 = \mathbf{S}_0 : \frac{1}{2}\dot{\mathbf{C}} \tag{24}$$

where $\mathbf{S}_0$ is a second P-K stress:

$$\mathbf{S}_0 = \mathbf{F}^{-1}\boldsymbol{\tau}_0\mathbf{F}^{-\mathrm{T}} \tag{25}$$

With the decomposition of the velocity gradient $\mathbf{L}_I$ (see Eq. (8)), $P_I$ can be further split into an elastic part $P_I^e$ and an inelastic part $P_I^i$:

$$P_I = P_I^e + P_I^i \tag{26}$$

where

$$P_I^e = \boldsymbol{\tau}_I : \mathbf{L}_I^e = \boldsymbol{\tau}_I : \mathbf{D}_I^e = \boldsymbol{\tau}_I : \frac{1}{2}\mathbf{F}^{e-\mathrm{T}}\dot{\bar{\mathbf{C}}}_I^e\mathbf{F}^{e-1} = \bar{\mathbf{S}}_I^e : \frac{1}{2}\dot{\bar{\mathbf{C}}}_I^e \tag{27}$$

$$P_I^i = \boldsymbol{\tau}_I : \mathbf{L}_I^i = \boldsymbol{\tau}_I : \mathbf{F}^e\bar{\mathbf{L}}_I^i\mathbf{F}^{e-1} = \bar{\mathbf{M}}_I^e : \bar{\mathbf{L}}_I^i \tag{28}$$

From the above two equations a second P-K stress $\bar{\mathbf{S}}_I^e$ and a Mandel stress $\bar{\mathbf{M}}_I^e$ defined in $\bar{\Omega}$ can be obtained:

$$\bar{\mathbf{S}}_I^e = \mathbf{F}^{e-1}\boldsymbol{\tau}_I\mathbf{F}^{e-\mathrm{T}} \tag{29}$$

$$\bar{\mathbf{M}}_I^e = \mathbf{F}^{e\mathrm{T}}\boldsymbol{\tau}_I\mathbf{F}^{e-\mathrm{T}} = \bar{\mathbf{C}}_I^e\bar{\mathbf{S}}_I^e \tag{30}$$

$\bar{\mathbf{M}}_I^e$ represents the driving stress for the inelastic deformation, and it is assumed to be additively split into two parts as:

$$\bar{\mathbf{M}}_I^e = \bar{\mathbf{M}}_I^v + \bar{\mathbf{M}}_I^a \tag{31}$$

where $\bar{\mathbf{M}}_I^v$ is a viscous stress that represents the LYR; $\bar{\mathbf{M}}_I^a$ is a viscoelastic back stress that represents the GNR. Then $P_I^i$ is also additively split into two parts as:

$$P_I^i = P_I^v + P_I^a \tag{32}$$

where $P_I^v = \bar{\mathbf{M}}_I^v : \bar{\mathbf{L}}_I^i = \bar{\mathbf{M}}_I^v : \bar{\mathbf{D}}_I^i$ and $P_I^a = \bar{\mathbf{M}}_I^a : \bar{\mathbf{L}}_I^i = \bar{\mathbf{M}}_I^a : \bar{\mathbf{D}}_I^i$.

With Eqs. (23), (24), (26), (27) and (32), the stress power $P$ is finally additively decomposed into seven parts:

$$\begin{aligned} P = {} & \mathbf{S}_0 : \frac{1}{2}\dot{\mathbf{C}} + \bar{\mathbf{S}}_1^e : \frac{1}{2}\dot{\bar{\mathbf{C}}}_1^e + \bar{\mathbf{S}}_2^e : \frac{1}{2}\dot{\bar{\mathbf{C}}}_2^e \\ & + \bar{\mathbf{M}}_1^v : \bar{\mathbf{D}}_1^i + \bar{\mathbf{M}}_1^a : \bar{\mathbf{D}}_1^i + \bar{\mathbf{M}}_2^v : \bar{\mathbf{D}}_2^i + \bar{\mathbf{M}}_2^a : \bar{\mathbf{D}}_2^i \end{aligned} \tag{33}$$

Hence, the Clausius-Duhem inequality becomes

$$\begin{aligned} & \left( \mathbf{S}_0 - 2\frac{\partial \widehat{\psi}_0}{\partial \mathbf{C}} \right) : \frac{1}{2}\dot{\mathbf{C}} + \left( \bar{\mathbf{S}}_1^e - 2\frac{\partial \widehat{\psi}_1^e}{\partial \bar{\mathbf{C}}_1^e} \right) : \frac{1}{2}\dot{\bar{\mathbf{C}}}_1^e + \left( \bar{\mathbf{S}}_2^e - 2\frac{\partial \widehat{\psi}_2^e}{\partial \bar{\mathbf{C}}_2^e} \right) : \frac{1}{2}\dot{\bar{\mathbf{C}}}_2^e \\ & + \left( \bar{\mathbf{M}}_1^a - 2\frac{\partial \widehat{\psi}_1^a}{\partial \bar{\mathbf{A}}_1}\dot{\bar{\mathbf{A}}}_1 \right) : \bar{\mathbf{D}}_1^i + \left( \bar{\mathbf{M}}_2^a - 2\frac{\partial \widehat{\psi}_2^a}{\partial \bar{\mathbf{A}}_2}\dot{\bar{\mathbf{A}}}_2 \right) : \bar{\mathbf{D}}_2^i + \bar{\mathbf{M}}_1^v : \bar{\mathbf{D}}_1^i \\ & + \bar{\mathbf{M}}_2^v : \bar{\mathbf{D}}_2^i + \frac{\partial \widehat{\psi}_1^a}{\partial \bar{\mathbf{A}}_1} : \mathbf{f}_1\left(\boldsymbol{\Lambda}_1\right) + \frac{\partial \widehat{\psi}_2^a}{\partial \bar{\mathbf{A}}_2} : \mathbf{f}_2\left(\boldsymbol{\Lambda}_2\right) \geq 0 \end{aligned} \tag{34}$$

According to the Coleman-Noll argument, the following stress relations can be obtained from the first five terms of the above inequality:

$$\mathbf{S}_0 = 2\frac{\partial \widehat{\psi}_0}{\partial \mathbf{C}} \tag{35}$$

$$\bar{\mathbf{S}}_1^e = 2\frac{\partial \widehat{\psi}_1^e}{\partial \bar{\mathbf{C}}_1^e} \tag{36}$$

$$\bar{\mathbf{S}}_2^e = 2\frac{\partial \widehat{\psi}_2^e}{\partial \bar{\mathbf{C}}_2^e} \tag{37}$$

$$\bar{\mathbf{M}}_1^a = 2\frac{\partial \widehat{\psi}_1^a}{\partial \bar{\mathbf{A}}_1}\dot{\bar{\mathbf{A}}}_1 \tag{38}$$

$$\bar{\mathbf{M}}_2^a = 2\frac{\partial \widehat{\psi}_2^a}{\partial \bar{\mathbf{A}}_2}\dot{\bar{\mathbf{A}}}_2 \tag{39}$$

All the above stresses are symmetric. In addition, since $\bar{\mathbf{S}}_I^e$ and $\bar{\mathbf{C}}_I^e$ commute, the Mandel stresses $\bar{\mathbf{M}}_I^e$ and $\bar{\mathbf{M}}_I^v$ are also symmetric.

Using Eqs. (35)~(39), the Clausius-Duhem inequality is finally reduced to the following dissipation inequality:

$$\bar{\mathbf{M}}_1^v : \bar{\mathbf{D}}_1^i + \bar{\mathbf{M}}_2^v : \bar{\mathbf{D}}_2^i + \frac{\partial \widehat{\psi}_1^a}{\partial \bar{\mathbf{A}}_1} : \mathbf{f}_1\left(\mathbf{\Lambda}_1\right) + \frac{\partial \widehat{\psi}_2^a}{\partial \bar{\mathbf{A}}_2} : \mathbf{f}_2\left(\mathbf{\Lambda}_2\right) \geq 0 \tag{40}$$

which can be satisfied by

$$\bar{\mathbf{M}}_I^v : \bar{\mathbf{D}}_I^i \geq 0 \tag{41}$$

and

$$\bar{\mathbf{M}}_I^a : \mathbf{f}_I\left(\mathbf{\Lambda}_I\right)\bar{\mathbf{A}}_I^{-1} \geq 0 \tag{42}$$

The inequality (41) will be satisfied by the flow rule for $\bar{\mathbf{D}}_I^i$, while the inequality (42) will be satisfied by the function $\mathbf{f}_I\left(\mathbf{\Lambda}_I\right)$.

### 3.4. Constitutive equations

#### 3.4.1. Specification of the free energy functions

Both $\widehat{\psi}_1^e$ and $\widehat{\psi}_2^e$ are modeled by the following strain energy function (Ames et al., 2009):

$$\widehat{\psi}_I^e\left(\bar{\mathbf{C}}_I^e\right) = \widehat{\psi}_I^e\left(\bar{\mathbf{E}}_I^e\right) = \mu_I^e\left\|\bar{\mathbf{E}}_I^e\right\|^2 + \frac{1}{2}\left(\kappa_I^e - \frac{2}{3}\mu_I^e\right)\left(\mathrm{tr}\bar{\mathbf{E}}_I^e\right)^2 \tag{43}$$

where $\bar{\mathbf{E}}_I^e = \ln\left(\bar{\mathbf{U}}_I^e\right)$ is a logarithmic elastic strain, $\mu_I^e$ is a shear modulus, $\kappa_I^e$ is a bulk modulus and the symbol $\|\bullet\|$ denotes the Frobenius norm, namely, $\left\|\bar{\mathbf{E}}_I^e\right\| = \sqrt{\bar{\mathbf{E}}_I^e : \bar{\mathbf{E}}_I^e}$. Then, with Eqs. (29), (30), (36) and (37), the Mandel stress $\bar{\mathbf{M}}_I^e$ and the Kirchhoff stress $\boldsymbol{\tau}_I$ can be obtained as

$$\bar{\mathbf{M}}_I^e = 2\mu_I^e \mathrm{dev}\left[\bar{\mathbf{E}}_I^e\right] + \kappa_I \left(\mathrm{tr}\bar{\mathbf{E}}_I^e\right)\mathbf{I} \tag{44}$$

$$\boldsymbol{\tau}_I = \mathbf{F}^{e-\mathrm{T}} \bar{\mathbf{M}}_I^e \mathbf{F}^{e\mathrm{T}} \tag{45}$$

Given the Young's modulus $E_I^e$ and the Poisson's ratio $\nu_I^e$, $\mu_I^e$ and $\kappa_I^e$ equal to

$$\mu_I^e = \frac{E_I^e}{2\left(1+\nu_I^e\right)}, \quad \kappa_I^e = \frac{E_I^e}{3\left(1-2\nu_I^e\right)} \tag{46}$$

For the sake of simplicity, it is assumed that $\nu_1^e = \nu_2^e = \nu$ here.

To specify the free energy functions for $\hat{\psi}_1^a$ and $\hat{\psi}_2^a$, it is assumed that $\det\left(\bar{\bar{\mathbf{A}}}_I\right) = 1$ and $\hat{\psi}_I^a$ follows the Neo-Hookean form:

$$\hat{\psi}_I^a\left(\bar{\mathbf{A}}_I\right) = \frac{1}{2}\mu_I^a\left(tr\bar{\mathbf{A}}_I - 3\right) \tag{47}$$

where $\mu_I^a$ is a shear modulus for modeling the GNR. Then with Eqs. (38) and (39), the following can be obtained:

$$\bar{\mathbf{M}}_I^a = \mu_I^a\left(\bar{\mathbf{A}}_I - \omega_I^a\mathbf{I}\right) \tag{48}$$

with $\omega_I^a$ a Lagrange multiplier (Guo et al., 2018). Assume $\bar{\mathbf{M}}_I^a$ is deviatoric, then $\omega_I^a = \frac{1}{3}\mathrm{tr}\bar{\mathbf{A}}_I$ and

$$\bar{\mathbf{M}}_I^a = \mu_I^a \mathrm{dev}\left[\bar{\mathbf{A}}_I\right] \tag{49}$$

With Eqs. (31), (44) and (49), the Mandel stresses $\bar{\mathbf{M}}_I^v$ is derived as

$$\bar{\mathbf{M}}_I^v = 2\mu_I^e \mathrm{dev}\left[\bar{\mathbf{E}}_I^e\right] - \mu_I^a \mathrm{dev}\left[\bar{\mathbf{A}}_I\right] + \kappa_I \left(\mathrm{tr}\bar{\mathbf{E}}_I^e\right)\mathbf{I} \tag{50}$$

Thus, $\bar{\mathbf{M}}_I^v$ is not deviatoric. The deviatoric part of $\bar{\mathbf{M}}_I^v$ equals to

$$\bar{\mathbf{M}}_I^i = \mathrm{dev}\left[\bar{\mathbf{M}}_I^v\right] = 2\mu_I^e \mathrm{dev}\left[\bar{\mathbf{E}}_I^e\right] - \mu_I^a \mathrm{dev}\left[\bar{\mathbf{A}}_I\right] \tag{51}$$

which is the effective Mandel stress power-conjugated to the inelastic deformation rate $\bar{\mathbf{D}}_I^i$ and will be used in defining the flow rule.

Then, to model the RNR, the argument of Ames et al. (2009) and the Gent free energy function are employed for $\hat{\psi}_0$:

$$\hat{\psi}_0\left(\mathbf{C}\right) = \hat{\psi}_0\left(\mathbf{C}_{dis}, J\right) = \frac{1}{2}\mu_0 I_m \ln\left(1 - \frac{I^* - 3}{I_m}\right) + \frac{1}{2}\kappa_0 \left(\ln J\right)^2 \tag{52}$$

where $\mathbf{C}_{dis} = \mathbf{F}_{dis}^T \mathbf{F}_{dis} = J^{-2/3}\mathbf{C}$ is the distortional part of $\mathbf{C}$ ($\mathbf{F}_{dis} = J^{-1/3}\mathbf{F}$ is the distortional part of $\mathbf{F}$), $I^* = \mathrm{tr}\mathbf{C}_{dis}$ is the first principle invariant of $\mathbf{C}_{dis}$, while $\mu_0$, $\kappa_0$ and $I_m$ represent the initial shear modulus, the bulk modulus and the limited extensibility, respectively. Since the volumetric elastic energy in $\hat{\psi}_0$ should be much less than that in $\hat{\psi}_I^e$, it is assumed that $\kappa_0 = 0$. Thus, with Eqs. (25), (35) and (52), the Kirchhoff stress $\boldsymbol{\tau}_0$ can be obtained:

$$\boldsymbol{\tau}_0 = \mu_0 \left(1 - \frac{\mathrm{tr}\mathbf{B}_{dis} - 3}{I_m}\right)^{-1} \mathrm{dev}\left[\mathbf{B}_{dis}\right] \tag{53}$$

where $\mathbf{B}_{dis} = \mathbf{F}_{dis}\mathbf{F}_{dis}^T = J^{-2/3}\mathbf{B}$.

3.4.2. Flow rules and evolution equations

Firstly, to satisfy the dissipation inequality (41), the inelastic deformation rate $\bar{\mathbf{D}}_I^i$ is

defined by the following general flow rule:

$$\bar{\mathbf{D}}_I^i = d_I^i \bar{\mathbf{N}}_I^i \text{, with } d_I^i = \left\| \bar{\mathbf{D}}_I^i \right\| \text{ and } \bar{\mathbf{N}}_I^i = \frac{\bar{\mathbf{M}}_I^i}{\left\| \bar{\mathbf{M}}_I^i \right\|} \tag{54}$$

By defining the equivalent shear stress $\tau_I^i = \frac{1}{\sqrt{2}} \left\| \bar{\mathbf{M}}_I^i \right\|$ and the equivalent shear strain rate $\dot{\gamma}_I^i = \sqrt{2} d_I^i$, the flow rule becomes

$$\bar{\mathbf{D}}_I^i = \frac{1}{\sqrt{2}} \dot{\gamma}_I^i \bar{\mathbf{N}}_I^i = \frac{\dot{\gamma}_I^i}{2\tau_I^i} \bar{\mathbf{M}}_I^i \tag{55}$$

Then, to satisfy the dissipation inequality (42) and recalling the two main aspects (the distortion of the glassy network and the molecular mobility of the yielded regions) that govern the relaxation of the GNR, $\mathbf{f}_I\left(\boldsymbol{\Lambda}_I\right)$ is given as

$$\mathbf{f}_I\left(\boldsymbol{\Lambda}_I\right) = f_I\left(\bar{\boldsymbol{\Lambda}}_I\right) \bar{\mathbf{M}}_I^a \bar{\mathbf{A}}_I \tag{56}$$

where $\bar{\mathbf{M}}_I^a \bar{\mathbf{A}}_I$ models the effect of the distortion of the glassy network itself on its relaxation while $f_I\left(\bar{\boldsymbol{\Lambda}}_I\right) \geq 0$ is a scalar-valued function of $\bar{\boldsymbol{\Lambda}}_I$ ($\bar{\boldsymbol{\Lambda}}_I \subseteq \boldsymbol{\Lambda}_I$) and models the effect of the molecular mobility (relaxation rate) of the yielded regions on the relaxation of the distorted glassy network. The experimental phenomena imply that $f_I\left(\bar{\boldsymbol{\Lambda}}_I\right)$ should be strain- and strain-rate-dependent and is assumed to be:

$$f_I\left(\bar{\boldsymbol{\Lambda}}_I\right) = f_r\left(\dot{\gamma}_I^i, \bar{\gamma}_I^i, \beta_I\right) = h_I \dot{\gamma}_I^i + g_I \beta_I \tag{57}$$

where $h_I \geq 0$ is a material parameter, $g_I = g_I\left(\bar{\gamma}_I^i\right)$ is a function of the accumulated inelastic shear strain $\bar{\gamma}_I^i = \int_0^t \dot{\gamma}_I^i dt$, and $\beta_I$ is a state variable associated with the deformation rate. In Eq. (57), the first term is introduced to model the saturation value of the GNR; the second term is introduced to model the strain- and strain-rate-dependent relaxation of the GNR. With

Eqs. (19), (56) and (57), the evolution equation for $\bar{\mathbf{A}}_I$ can be written as

$$\dot{\bar{\mathbf{A}}}_I = \bar{\mathbf{D}}_I^i \bar{\mathbf{A}}_I + \bar{\mathbf{A}}_I \bar{\mathbf{D}}_I^i - h_I \dot{\gamma}_I^i \bar{\mathbf{M}}_I^a \bar{\mathbf{A}}_I - g_I \beta_I \bar{\mathbf{M}}_I^a \bar{\mathbf{A}}_I \tag{58}$$

Considering the significant strain dependence of stress relaxation around the yield peak, the following exponential function is chosen for $g_I$:

$$g_I\left(\bar{\gamma}_I^i\right) = g_{I*}\left\{1 - \exp\left[-\left(\frac{\bar{\gamma}_I^i}{\bar{\gamma}_g^i}\right)^2\right]\right\} \tag{59}$$

where $g_{I*}$ and $\bar{\gamma}_g^i$ are material parameters. Furthermore, considering that the strain-rate dependence of stress relaxation and the molecular mobility of a glassy polymer after yield is significantly increased, $\beta_I$ is assumed to be a relaxation rate dominated by the inertia motion of the molecules. This assumption is made based on an analogy to the inertia-motion-dominated fast relaxation process observed in glassy-forming liquids (Pazmino Betancourt et al., 2018). Although in glassy-forming liquids the relaxation time for the fast relaxation process is only on the order of picoseconds, it is reasonable to make the analogy since the yielding of a glassy polymer can be regarded as glass transition taking place in presence of large deformation (Liu et al., 2015). The physics for the inertia-motion-dominated stress relaxation of glassy polymers needs to be further clarified in the future. In this research, it is assumed that the inertia motion is determined by the history of the inelastic strain rate $\dot{\gamma}_I^i$; hence, a phenomenological equation which relates the inertia motion and the inertia-motion-dominated relaxation rate is proposed for the evolution of $\beta_I$:

$$\dot{\beta}_I = \frac{\dot{\gamma}_I^i - \chi \beta_I}{t^n} \tag{60}$$

where $\chi > 0$ and $0 < n \le 1$ are material parameters, and $t$ is the time.

Up to now, the equivalent shear strain rate $\dot{\gamma}_I^i$ must be specified to complete the constitutive description.

Firstly, $\dot{\gamma}_1^i$ is given by the following modified Argon viscoplastic law to model the rate-dependent yield and flow:

$$\dot{\gamma}_1^i = \dot{\gamma}_{1*}^i \left[ \exp\left( \frac{A}{T}\left(\tau_1^i - s_1\right)\right) - \exp\left( -\frac{A}{T} s_1 \right)\right] \tag{61}$$

where $\dot{\gamma}_{1*}^i$ is a pre-exponential factor, $A$ is proportional to the activation volume, $T$ is the absolute temperature and $s_1$ is a shear stress determined by the LYR of the entangled chains. $s_1$ is assumed to equal to

$$s_1 = s_s + s_h + \alpha_p p \tag{62}$$

where $s_s$ and $s_h$ are internal variables introduced to model the strain softening and isotropic hardening behaviors of the glassy polymer. Additionally, the term $\alpha_p p$ is used to include the pressure effect, where $\alpha_p \geq 0$ is a pressure-dependence factor and $p$ is the mean normal pressure defined by

$$p = -\frac{1}{3}\mathrm{tr}\left(\bar{\mathbf{M}}_1^e + \bar{\mathbf{M}}_2^e\right) \tag{63}$$

The evolution equations for $s_s$ and $s_h$ are given by

$$\dot{s}_s = h_{ss}\left(1 - \frac{s_s}{s_{seq}}\right)\dot{\gamma}_1^i, \text{ with } s_s(0) = s_{s*} \tag{64}$$

$$\dot{s}_h = h_{sh}\left(\lambda_1^{iEff} - 1\right)\left(1 - \frac{s_h}{s_{heq}}\right)\dot{\gamma}_1^i, \text{ with } s_h(0) = 0 \tag{65}$$

where $h_{ss}$, $s_{seq}$, $s_{s*}$, $h_{sh}$ and $s_{heq}$ are material parameters, and $\lambda_1^{iEff}$ is an effective stretch defined as

$$\lambda_1^{iEff} = \sqrt{\frac{1}{3}\mathrm{tr}\bar{\mathbf{B}}_1^i} \tag{66}$$

Secondly, $\dot{\gamma}_2^i$ is given by the following power law:

$$\dot{\gamma}_2^i = \dot{\gamma}_{2*}^i \left( \frac{\tau_2^i}{s_2} \right)^{\frac{1}{m}} \tag{67}$$

where $\dot{\gamma}_{2*}^i = 1$ is a rate-dimensioned factor, $0 < m \le 1$ is a rate-sensitivity parameter and $s_2$ is a shear stress determined by the LYR of the non-entangled chains.

Finally, since the stiffness of a glassy polymer observed during unloading significantly depends on the applied strain, the evolution of the tangent moduli in deformation should be modeled to achieve better prediction of the strain recovery. As argued by Ayoub et al. (2010), the strain-dependent stiffness can be attributed to two physical phenomena playing opposite effects: damage-induced stiffness decrease and chain-alignment-induced stiffness increase. Because the stiffness increase has already been considered by the Gent model, it only needs to model the stiffness decrease here. Since the non-entangled chains are usually short and its stiffness may be much higher than the secondary bonds, it is assumed that $E_2^e$ is governed by the secondary bonds and is independent of the strain, namely,

$$E_2^e = E_{2*}^e \tag{68}$$

where $E_{2*}^e$ is the initial value of $E_2^e$. While the decrease of $\mu_1^a$, $\mu_2^a$ and $E_2^e$ are assumed to be modeled by the following empirical functions, respectively:

$$\mu_1^a = \mu_{1*}^a \left(1 - D_1^a\right) \tag{69}$$

$$\mu_2^a = \mu_{2*}^a \left(1 - D_2^a\right) \tag{70}$$

$$E_1^e = E_{1*}^e \left(1 - D_1^e\right) \tag{71}$$

where $\mu_{1*}^{a}$, $\mu_{2*}^{a}$ and $E_{1*}^{e}$ denote the initial values of the moduli; $D_1^a$, $D_2^a$ and $D_1^e$ are three damage fractions given by:

$$D_1^a = D_{1eq}^a \left[ 1 - \exp\left( -\frac{\overline{\gamma}_1^i}{\overline{\gamma}_1^a} \right) \right] \tag{72}$$

$$D_2^a = D_{2eq}^a \left[ 1 - \exp\left( -\frac{\overline{\gamma}_2^i}{\overline{\gamma}_2^a} \right) \right] \tag{73}$$

$$D_1^e = D_{1eq}^e \left[ 1 - \exp\left( -\frac{\overline{\gamma}_1^i}{\overline{\gamma}_1^e} \right) \right] \tag{74}$$

where $D_{1eq}^a$, $D_{2eq}^a$, $D_{1eq}^e$, $\overline{\gamma}_1^a$, $\overline{\gamma}_2^a$ and $\overline{\gamma}_1^e$ are material parameters. $0 \le D_{1eq}^a < 1$, $0 \le D_{2eq}^a < 1$ and $0 \le D_{1eq}^e < 1$ denote the saturation values of the damage fractions.

## 4. Model calibration and material parameters

### 4.1. Fitting of the present model with experimental data

The present model was implemented for uniaxial loading conditions in the computer program MATLAB with an explicit algorithm. The differential equations are solved with the ode45 Solver. The material parameters were obtained by fitting the experimental data to the model. A heuristic calibration procedure is presented in Appendix A and the calibrated parameters for the PC glass are listed in Table 1. To model the strain recovery behavior, at least two stress-strain curves with a loading-unloading-recovery cycle are needed for the calibration. Considering the strain recovery before and after significant strain hardening is of distinct nature, the strains of 40% and 100% are chosen here. As demonstrated by Fig. 9a, the present model is capable of capture the initial stiffness, yield peak and strain hardening quite well. In addition, good fit can be achieved for the strain recovery during unloading and at zero stress across a wide strain range. Fig. 9b shows that the strain-rate-dependent yield and flow can also be satisfactorily captured by the present model. However, the present model

cannot well describe the strain hardening at the highest strain rate of $1\times10^{-1}$ $s^{-1}$; the reason may be that the thermal-mechanical coupling effect, which can soften the material by self-heating, is not included yet. Finally, to enable the present model to capture the post-yield stress relaxation behavior, as demonstrated by Fig. 9c~d, stress-time curves obtained from the stress-relaxation tests at different strains (at least one near the yield-peak and another one in the strain hardening region) are also needed for the calibration.

**Table 1**

Material parameters obtained for the present model based on the experimental data of the PC glass.

| Model parameter | Unit | Value | Remark |
|---|---|---|---|
| $E^e_{1*}$ | MPa | 800 | Elasticity |
| $E^e_{2*}$ | MPa | 1000 | |
| $\nu$ | - | 0.37 | |
| $s_2$ | MPa | 2 | Flow law (non-entangled chains) |
| $m$ | - | 0.2 | |
| $\dot{\gamma}^i_{1*}$ | $s^{-1}$ | $7.72\times10^{10}$ | Flow law (entangled chains) |
| $A$ | K/MPa | 403.7 | |
| $\alpha_p$ | - | 0.08 | Pressure sensitivity |
| $h_{ss}$ | MPa | 950 | Strain softening |
| $s_{s*}$ | MPa | 46 | |
| $s_{seq}$ | MPa | 30.5 | |
| $h_{sh}$ | MPa | 100 | Isotropic hardening |
| $s_{heq}$ | MPa | 10 | |
| $\mu^a_{1*}$ | MPa | 880 | GNR (entangled chains) |
| $h_1$ | - | 46 | |
| $g_{1*}$ | - | 1.1 | |
| $\mu^a_{2*}$ | MPa | 4000 | GNR (non-entangled chains) |
| $h_2$ | - | 240 | |
| $g_{2*}$ | - | 20 | |
| $\bar{\gamma}^i_g$ | - | 0.33 | GNR |
| $\chi$ | - | 0.2 | |
| $n$ | - | 0.56 | |

| | | | |
|---|---|---|---|
| $\mu_0$ | MPa | 13.8 | RNR |
| $I_m$ | - | 5.4 | |
| $D_{1eq}^a$ | - | 0.35 | Moduli evolution |
| $\overline{\gamma}_1^a$ | - | 0.14 | |
| $D_{2eq}^a$ | - | 0.7 | |
| $\overline{\gamma}_2^a$ | - | 0.21 | |
| $D_{1eq}^e$ | - | 0.55 | |
| $\overline{\gamma}_1^e$ | - | 1.13 | |

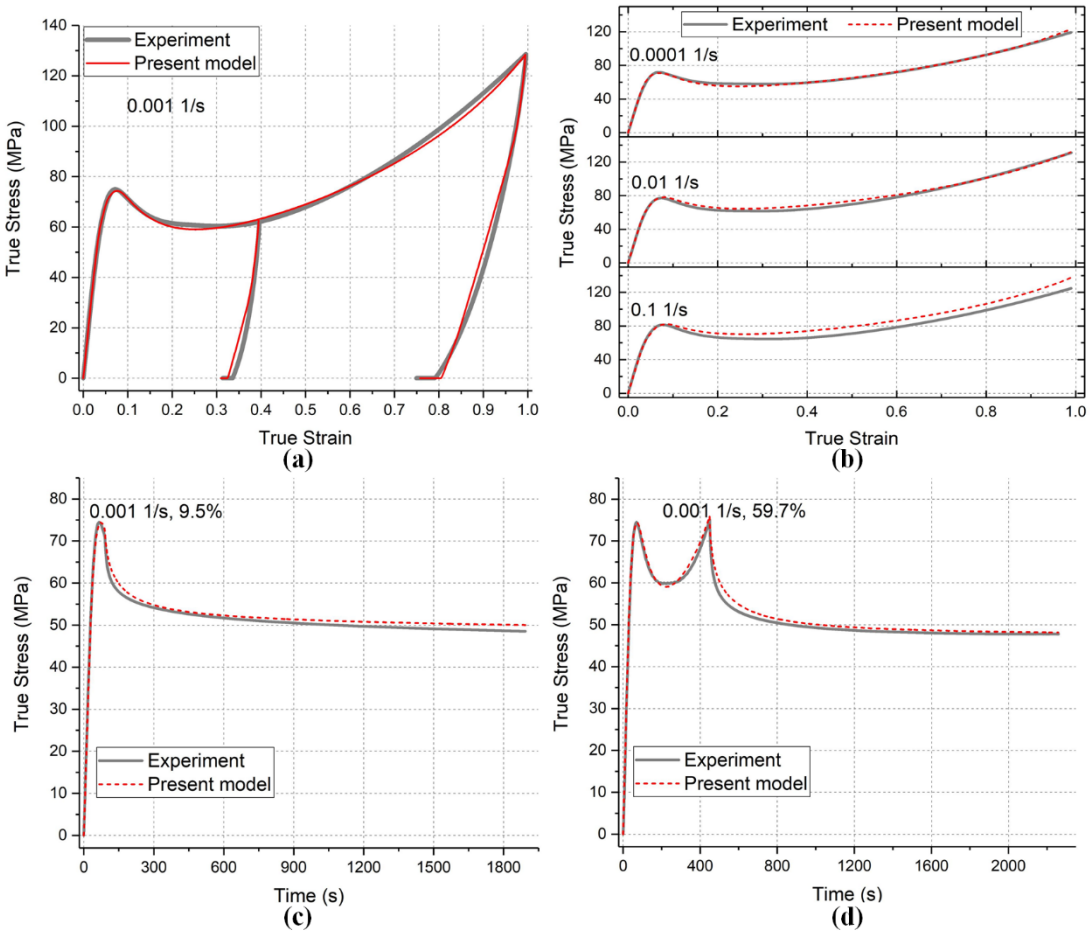


**Fig. 9.** Fitting of the present model with the experimental data of the PC glass: (a) stress-strain curves with a loading-unloading-recovery cycle at different strains, (b) stress-strain curves at different strain rates, and (c) ~ (d) stress-time curves of the stress-relaxation tests with different strains.

## 4.2. Fitting of the BPA and AAS models with experimental data

For purpose of comparison and discussion, the classical BPA model and the state-of-the-

art AAS model are also calibrated using the experimental data. Both the BPA and AAS models have been shown to be able to reproduce the strain-rate-dependent yield and flow. What's more, the AAS model have shown its capability in describing the unloading behavior at large strain. The calibrated constitutive parameters of the two models are given in Appendix B. Fig. 10 shows the fitting of the BPA and AAS models to the experimental stress-strain curves. The BPA model can acceptably capture the major characteristics of the loading curve except the yield peak and the strain-rate-dependent stress response at large strain. Calibration of the BPA model only requires the loading curves, however, the unloading behavior predicted by the model may be unrealistic. The AAS model can capture the loading-unloading-recovery behavior much better than the BPA model. With additional state variables to model the evolution of the yield strength, the AAS model can reproduce the loading curve almost perfectly. The strain-rate-dependent stress response at large strain can also be satisfactorily reproduced by the AAS model if the thermo-mechanical coupling effect and the rate-dependent Tg are considered. Calibration of the model requires both the loading and unloading curves, while the advantage obtained is that the strain recovered during unloading can be well-fitted. However, the predicted unloading curve is still of obvious discrepancy in comparison with the experimental data. Finally, it should be noted that both the BPA and AAS models can reproduce the phenomenon of strain recovery at zero stress if the RNR after unloading is still large enough to drive the reverse viscoplastic flow.

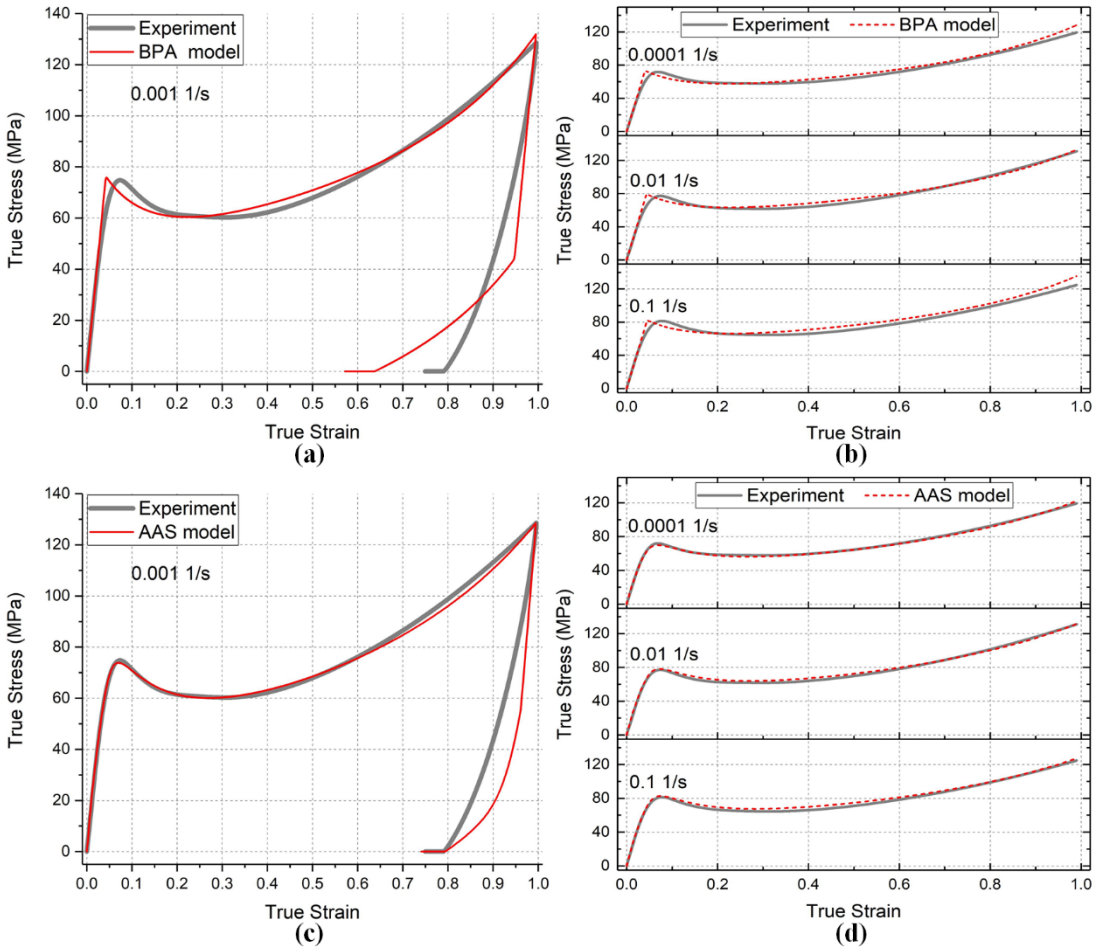


**Fig. 10.** Fitting of the BPA model ((a) ~ (b)) and the AAS model ((c) ~ (d)) with the experimental stress-strain curves of the PC glass: (a) or (c) the loading-unloading-recovery stress-strain behavior, and (b) or (d) the strain-rate-dependent yield and flow.

## 5. Model prediction and discussion

### 5.1. Stress relaxation behavior

Firstly, with the above calibrated models, simulations of strain-rate-dependent stress relaxation of the PC glass are discussed. Although with satisfactory prediction of the strain-rate-dependent yield and flow as presented in Fig. 10, both the BPA and AAS models fail to capture the stress relaxation behavior as shown in Fig. 11. The relaxed stress $\sigma_r$ predicted by the two models is 2~3 times less than the experimental value. In addition, the models predict nearly the same $\sigma_{inf}$ for cases of different strain rates, namely, the strain-rate-

dependent $\sigma_{inf}$ cannot be predicted by the two models. Thus, it can be concluded that, with the thermally-activated viscoplastic/viscous flow law alone, the strain-rate-dependent yield and flow and the strain-rate-dependent stress relaxation behavior in the post-yield region cannot be modeled at the same time. Namely, the "material clock" determined by the viscous/viscoplastic flow law that models the strain-rate-dependent yield and flow is different from the "material clock" that governs the stress relaxation behavior. While in the present model, with the consideration of the GNR, a viscoelastic back stress associated with the inelastic flow can be incorporated to solve this problem. As shown by Fig. 9 and Fig. 11, in the strain-rate range of $1\times10^{-4}$ to $1\times10^{-2}$ $s^{-1}$, the strain-rate-dependent yield and flow as well as the strain-rate-dependent stress relaxation behavior of the PC glass can be well reproduced by the present model. For the highest strain rate of $1\times10^{-1}$ $s^{-1}$, although there is still obvious discrepancy between the predicted and experimental relaxation curves, the present model can satisfactorily capture the values of $\sigma_r$ and $\sigma_{inf}$ as well as the overall stress relaxation process.

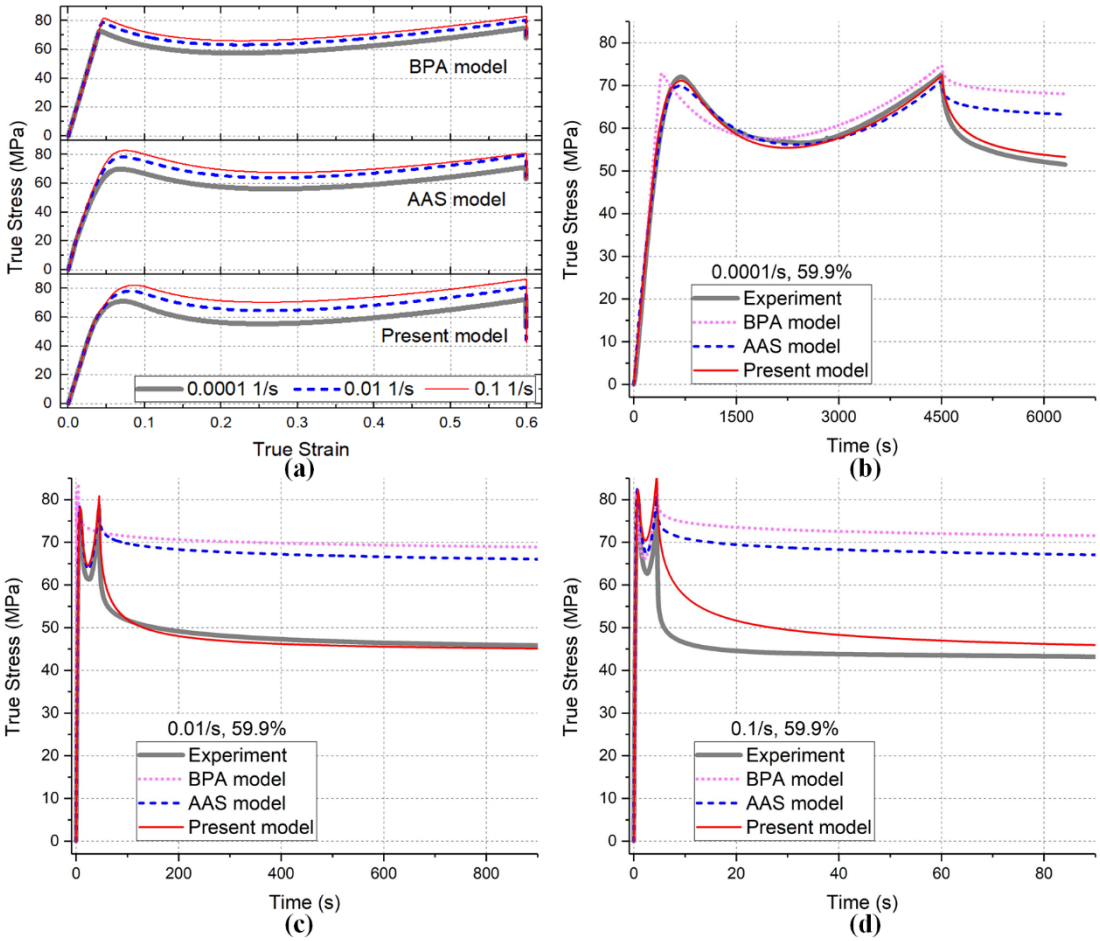


**Fig. 11.** Predictions by the models using the stress-relaxation tests of the PC glass at a strain of about 60% with different loading strain rates: (a) the predicted stress-strain curves, and (b) ~ (d) comparison of the predicted stress-time curves with experimental data.

Then, to check the predictive capability of the models for the strain-dependent stress relaxation of the PC glass, both stress-relaxation simulations and experimental tests were carried out at different strains. The loading process was controlled by a constant train rate of $1\times 10^{-2}$ $s^{-1}$ which had not been chosen for the calibration. Fig. 12 shows the stress-strain curves of the simulation results. Fig. 13 further shows the predicted stress-time curves and the comparison with the experimental data. Both the BPA and AAS model predict strain-independent stress relaxation in the post-yield region and fail to represent the strain-dependence in the strain softening region, while the present model can satisfactorily capture

this strain dependence.

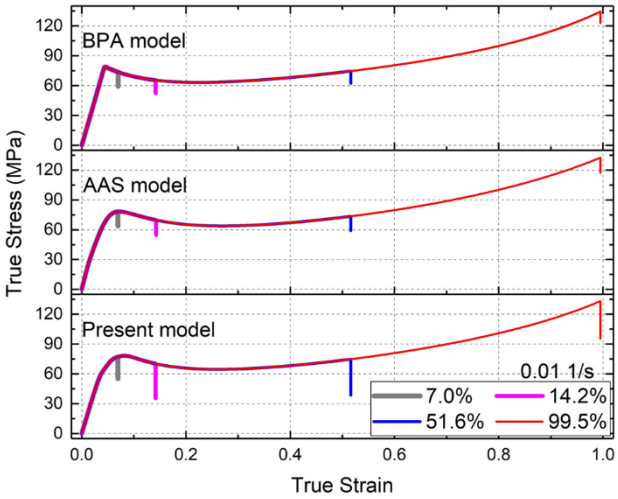


**Fig. 12.** The predicted stress-strain curves of the models for the stress-relaxation tests of the PC glass at different strains with a loading strain rate of $1\times10^{-2}$ $s^{-1}$.

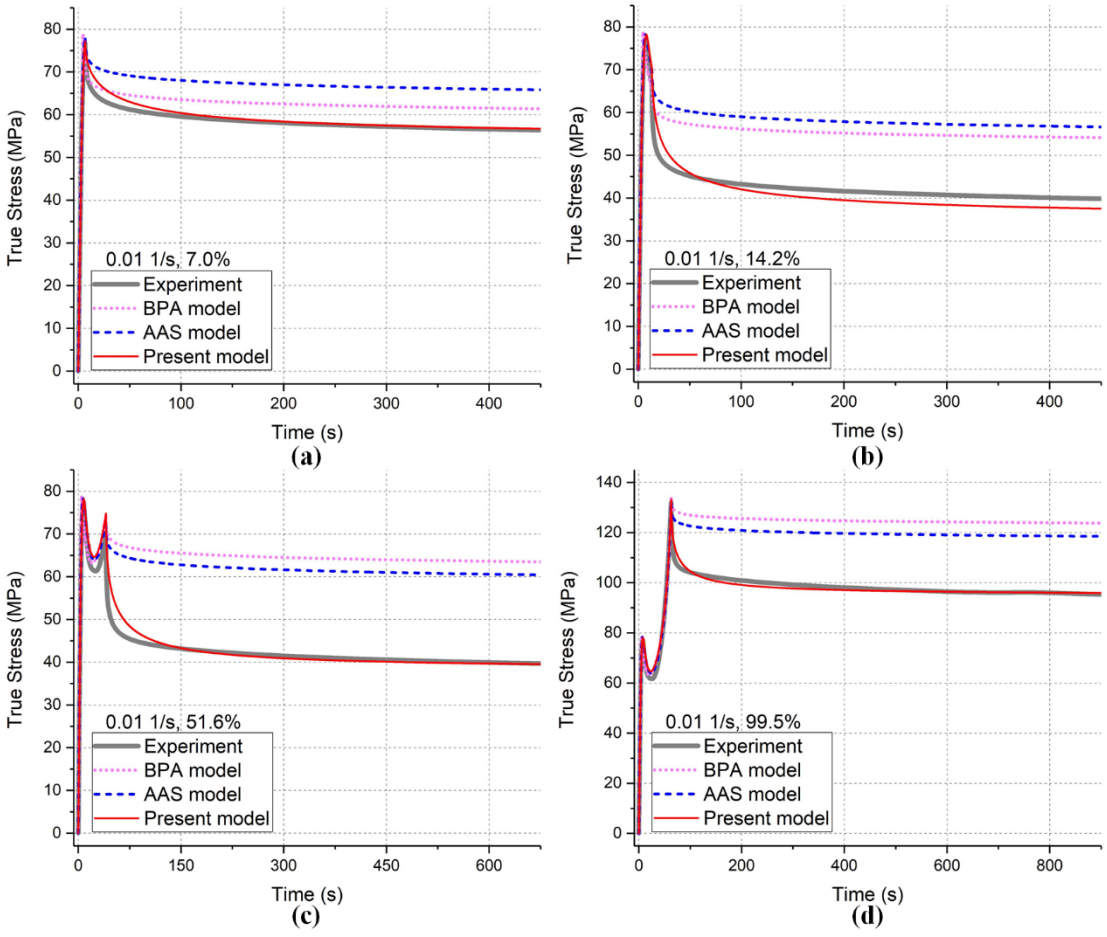

**Fig. 13.** The predicted stress-time curves of the models for stress-relaxation tests of the PC glass at different strains with a loading strain rate of $1\times10^{-2}$ $s^{-1}$ and the comparison with experimental data.

5.2. Loading-unloading-recovery behavior

Fig. 14 shows prediction using the present model for the loading-unloading-recovery behavior of the PC glass at a variety of post-yield strains, in which predictions using the BPA and AAS models are also displayed for comparison. In the strain-softening region (Fig. 14a-b), both the BPA and AAS models predict linear unloading curve and fail to capture the strain recovery at zero stress, leading to largely underestimated recovered strain. With the present model, although the strain recovered during unloading is still underestimated, the phenomena of strain recovery at zero stress can be satisfactorily captured. In addition, the nonlinear unloading curve can be reproduced when the strain is increased to the end of the strain-softening region. In the strain-hardening region (Fig. 14c-d), both the unloading curve and the recovered strain at zero stress can be well predicted by the present model. The BPA model is apt to overestimate the strain recovery once the reverse viscoplastic flow happens. The AAS model can reproduce more realistic unloading curve, however, it still predicts largely underestimated strain recovery. For most polymer models, the yielding process is modeled by the evolution of an internal variable which represents the yield strength. However, the yielding process is locally-started and with the elastic distortion of the glassy network. Thus, these models cannot satisfactorily reproduce the strain recovery in the post-yield region. In the present model, the roles of the GNR in controlling the yielding process is taken into consideration, which improves the accuracy in predicting the post-yield strain recovery significantly.

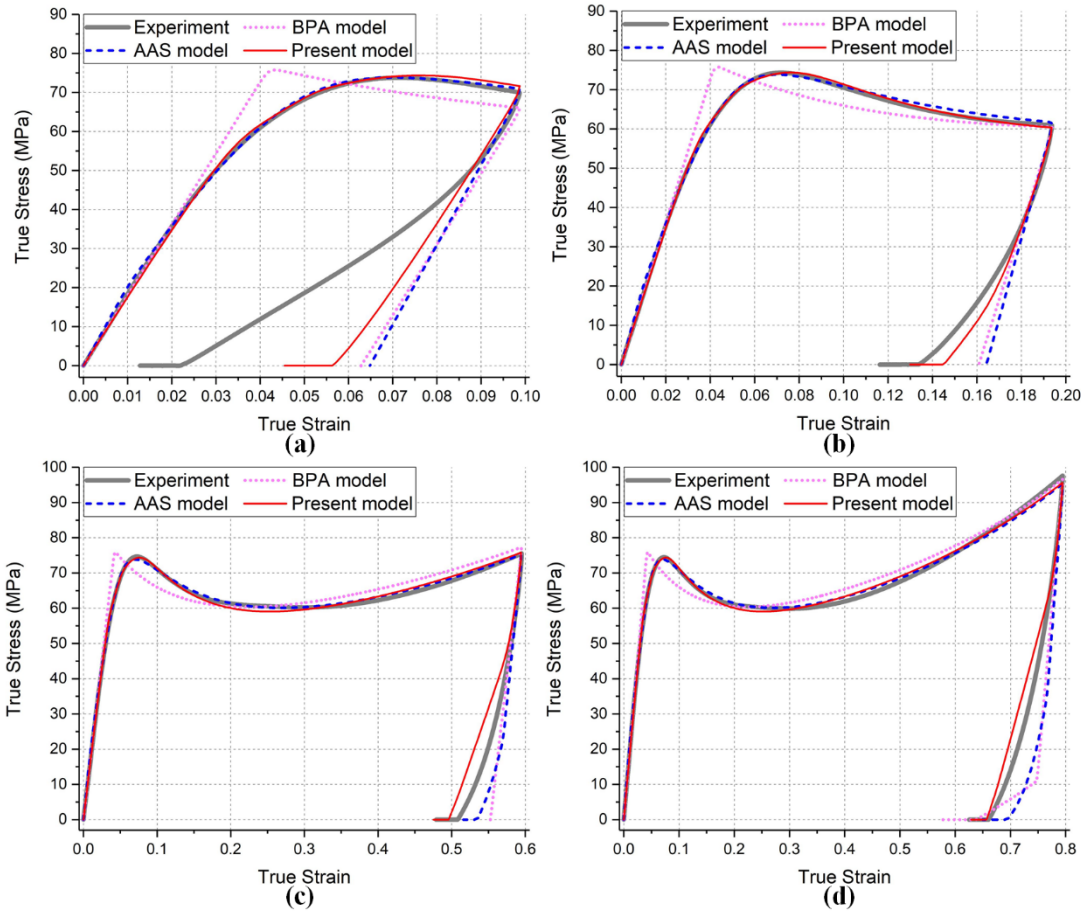


**Fig. 14.** Predictions using the models for the loading-unloading-recovery behavior of the PC glass at different strains and the comparison with experimental data: (a) 9.9%, (b) 19.4%, (c) 59.5% and (d) 79.5%. The strain rate employed is $1\times10^{-3}$ $s^{-1}$.

Furthermore, the predictive capability of the present model for the strain-rate dependence of loading-unloading-recovery behavior was illustrated in Fig. 15. With comparison to the experimental data (Fig. 6 and Fig. 7), it can be concluded that in the strain range of 20% ~ 100%, the nonlinear unloading behavior of the PC glass can be satisfactorily predicted by the present model. In the strain range of 20% ~ 100% (Fig. 15a-d), the strain-rate-dependent strain recovery at zero stress also can be satisfactorily predicted. As the strain is increased to about 100% (Fig. 15e-f), the strain recovered at zero stress for the highest strain rate of $1\times 10^{-1}$ $s^{-1}$ is significantly overestimated, which can be explained by the overestimated RNR as discussed in Section 4.1.

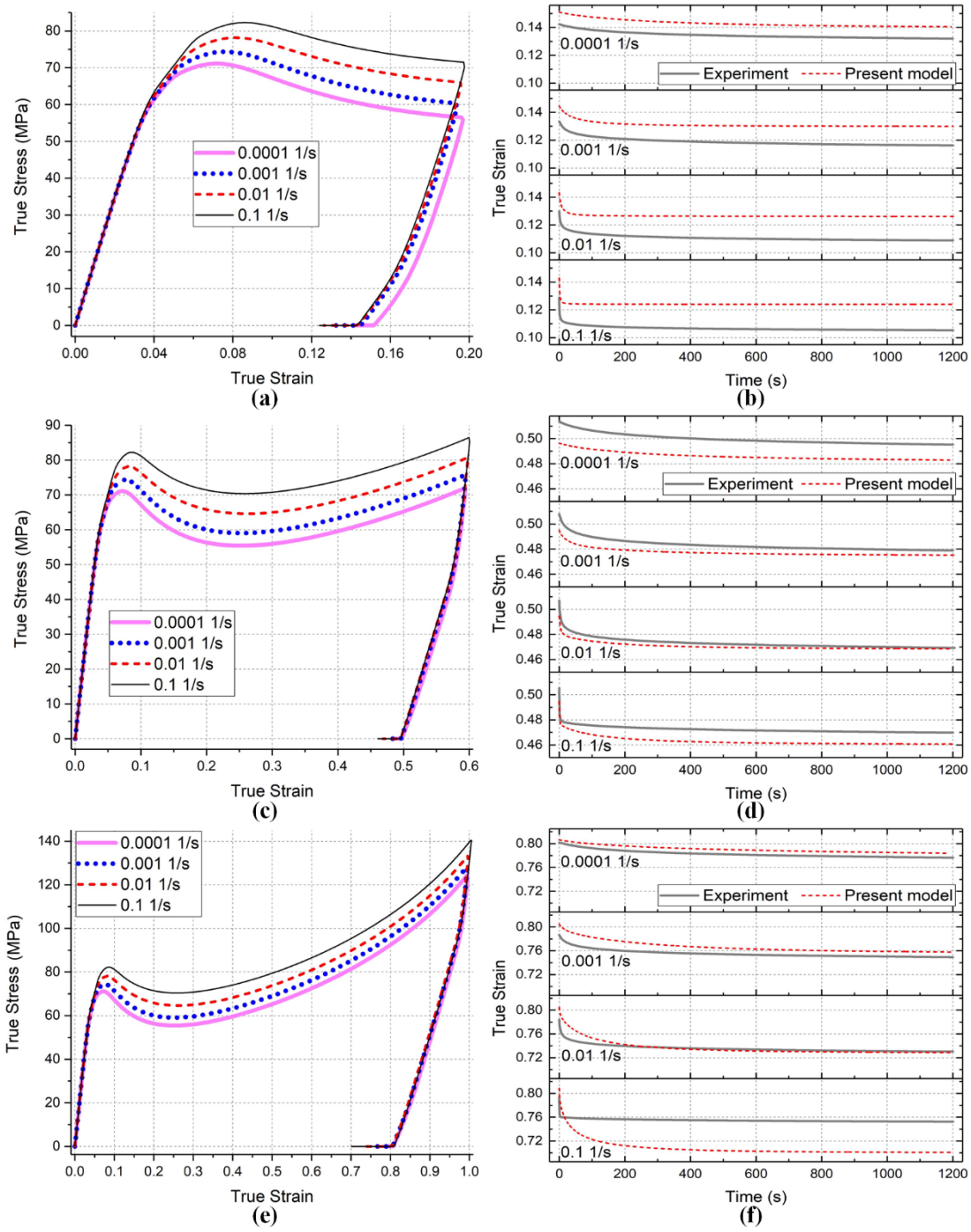


**Fig. 15.** Prediction using the present model for the strain-rate dependence of the loading-unloading-recovery behavior of the PC glass: (a), (c) and (e) are stress-strain curves, while (b), (d) and (f) are the corresponding recovered strain at zero stress with experimental data displayed for comparison.

Finally, a simulation of cyclic loading-unloading test of the PC glass in the post-yield region was conducted. The predicted stress-strain curve is compared with experimental data

as illustrated in Fig. 16. The hysteresis loops observed after strain softening can be satisfactorily represented by the present model, while the hysteresis loops observed at smaller strains near the yield peak cannot be modeled yet. Improvement of the present model for better representing the hysteresis loops as well as other viscoelastic response at small strains can be expected by incorporating more relaxation mechanisms.

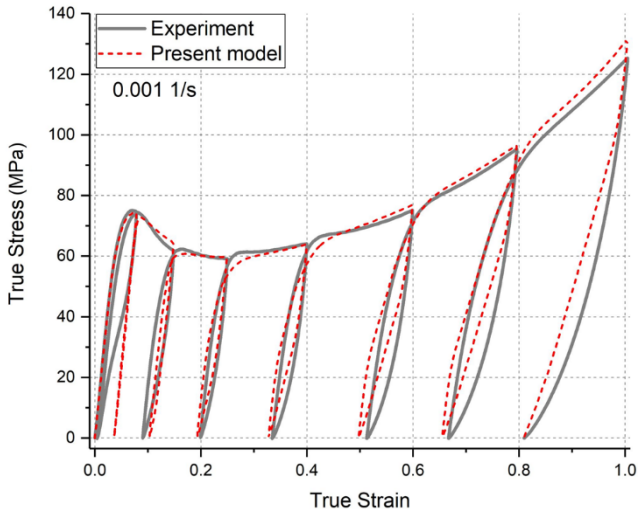


**Fig. 16.** Prediction using the present model for cyclic loading-unloading test of the PC glass in the post-yield region and the comparison with experimental data. The strain rate employed is $1\times10^{-3}$ $s^{-1}$.

## 6. Conclusions

Based on several recent investigations on the deformation of glassy polymers (Bending et al., 2014; Cheng and Wang, 2013; Kim et al., 2013; Li et al., 2018; Liu et al., 2015), this research further investigated and analyzed the important roles of the intrachain stress in controlling the yielding process as well as the post-yield deformation. In addition, a finite strain thermodynamically-based and physically-based constitutive model was proposed for representing the viscoelastic-viscoplastic (VE-VP) deformation behavior of glassy polymers, especially aiming at the stress relaxation and strain recovery in the post-yield region. According to the results of this research, the concluding remarks are listed as the following:

1. The deformation of a glassy polymer can be interpreted as the deformation of a glassy network linked by both the secondary bonds and the entanglements. The elastic distortion of the glassy network leads to an intrachain stress contribution, named as a glassy network resistance (GNR), to the macroscopic yield strength.
2. The GNR is distinct from the widely reported rubbery network resistance (RNR). The RNR mainly affects the strain hardening and strain recovery at large strain. The GNR is critical in controlling the yielding process and the post-yield deformation; its relaxation is dictated by the prior deformation rate and leads to the strain-rate-dependent stress relaxation and strain recovery behaviors.
3. The thermally-activated viscosity/viscoplasticity theory cannot rationalize the strain-rate-dependent characteristics of the VE-VP deformation behavior of glassy polymers. With the thermally-activated viscous/viscoplastic flow law alone, the strain-rate-dependent yield and flow and the strain-rate-dependent stress relaxation cannot be correctly modeled at the same time; the reason may be that the inertia motion of the molecules may affect the post-yield deformation significantly as the molecular mobility in a glassy polymer is significantly increased after yield.
4. With modeling of the GNR and its strain-rate-dependent relaxation in a simple phenomenological way, the constitutive model developed in this research can concurrently represent the stress relaxation and loading-unloading-recovery behaviors in the post-yield region, demonstrating great advantage for accurate and efficient modeling of the VE-VP deformation behavior of glassy polymers.

Considering limitations of the present model, there are some important improvements remained to be carried out. Firstly, more accurate modeling of the GNR is in urgent need. Both experimental investigations and molecular dynamics simulations are necessary to clarify

the underlying mechanisms and rules that govern the buildup and relaxation of the GNR, especially the effects of the inertia motion of the molecules. Secondly, the intricate coupling between the interchain and intrachain stresses is still mysterious and is challenging to be effectively represented by a constitute model. Finally, extension of the present model to non-isothermal conditions and taking the thermal-mechanical coupling effect into consideration are necessary to predict the VE-VP deformation behavior of glassy polymers over a wide temperature and strain-rate range.

## Acknowledgements

This work is supported by the project of G-SB91 from The Hong Kong Polytechnic University and the National Natural Science Foundation of China (51675334).

## Appendices

A. Calibration of material parameters in the present model

A.1. Discussion on the stress decomposition and evolution

To provide guidelines for the model calibration, a discussion on the stress decomposition and evolution was presented. As demonstrated by Fig A.1, the total stress $\boldsymbol{\sigma}$ is decomposed into a hyperelastic stress $\boldsymbol{\sigma}_0$ (for the RNR) and two inelastic stresses $\boldsymbol{\sigma}_1$ (for the IR due to the entangled chains) and $\boldsymbol{\sigma}_2$ (for the IR due to the non-entangled chains). The inelastic stress $\boldsymbol{\sigma}_I$ ($I = 1 \, or \, 2$) is further decomposed into a viscous part $\boldsymbol{\sigma}_I^i$ (for the LYR) and a viscoelastic part $\boldsymbol{\sigma}_I^a$ (for the GNR). With the increasing strain, $\boldsymbol{\sigma}_I$ is first increased to its peak value and then is decreased to a saturation value. The linear increase of $\boldsymbol{\sigma}_I$ models the initial stiffness. The decrease of $\boldsymbol{\sigma}_2$ starts before that of $\boldsymbol{\sigma}_1$ and models the transition of the stress-strain curve from the linear to the nonlinear region. The continued

nonlinear increase of $\boldsymbol{\sigma}_1$ models the pre-peak hardening, while the subsequent decrease of $\boldsymbol{\sigma}_1$ models the strain softening. In addition, the decrease of $\boldsymbol{\sigma}_2$ may also contribute to the strain softening. The strain hardening is modeled by the increase of $\boldsymbol{\sigma}_0$. At large strain, $\boldsymbol{\sigma}_1$ is increased again, which influences the strain hardening only slightly but is necessary for better modeling of the strain recovery.

The unloading curve is modeled by two distinct stages, which are determined by evolution of the stresses with decreasing external strain. As shown by Fig A.1(c) or (d), since the viscoelastic back stress $\boldsymbol{\sigma}_2^a$ is much larger than the viscous stress $\boldsymbol{\sigma}_2^i$, the reversed flow of the non-entangled chains starts shortly after the start of unloading. $\boldsymbol{\sigma}_2^a$ is firstly recovered to zero and then is increased in the reversed direction, which governs the first stage of the unloading curve. Once $\boldsymbol{\sigma}_2^a$ reaches its saturation value again, the unloading curve will enter the second stage which is governed by the evolution of $\boldsymbol{\sigma}_1$. As presented in A.1(e) or (f), the reversed flow of the network chains happens in the second stage, associated with which $\boldsymbol{\sigma}_1^a$ evolves in the same way as $\boldsymbol{\sigma}_2^a$ but may not be able to reach its saturation value. Since both $\boldsymbol{\sigma}_I^a$ reaches its saturation value in a nonlinear way, some nonlinear characteristics of the unloading curve can be satisfactorily captured.

The strain recovery at zero stress is modeled by the relaxation of $\boldsymbol{\sigma}_I$. With the relaxation of $\boldsymbol{\sigma}_2$, the reversed flow of the non-entangled chains will continue if the driven stress $\boldsymbol{\sigma}_1$ and $\boldsymbol{\sigma}_0$ is large enough. Similarly, with the relaxation of $\boldsymbol{\sigma}_2$, the reversed flow of the entangled chains will continue if the driven stress $\boldsymbol{\sigma}_0$ is large enough. For the strain of about 40%, only $\boldsymbol{\sigma}_2$ can be relaxed after unloading, thus the strain recovered at zero stress

mainly comes from the reversed flow of the non-entangled chain. For the strain of about 100%, both $\boldsymbol{\sigma}_1$ and $\boldsymbol{\sigma}_2$ can be relaxed after unloading, thus the reversed flows of both the entangled and non-entangled chains contribute to the strain recovery at zero stress. Hence, the present model can model the different nature of the strain recovery at zero stress for different strains.

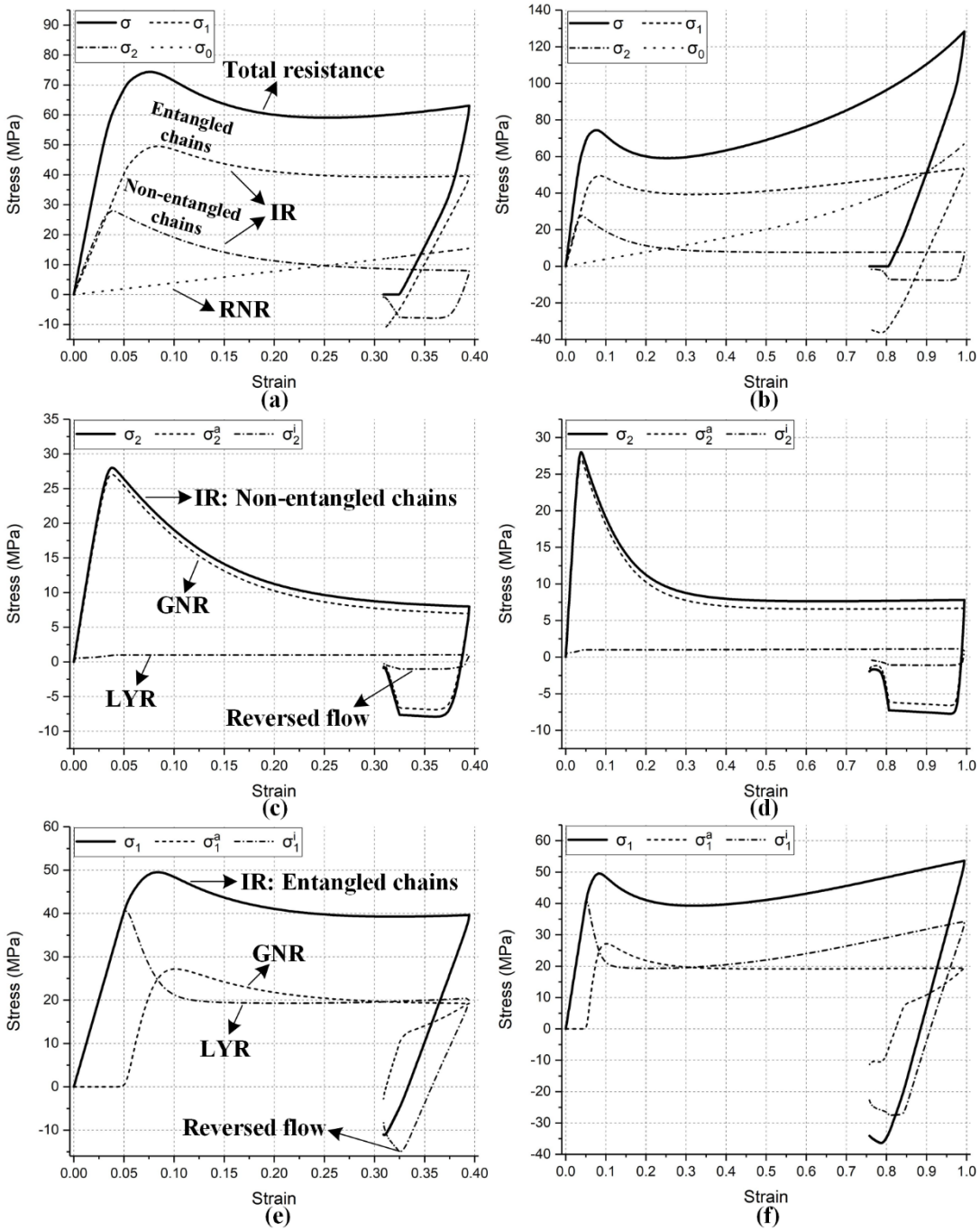

**Fig A.1** Decomposition of the total stress ((a) or (b)) and further decomposition of the inelastic stresses ((c) and (e) or (d) and (f)) and evolution of the stresses in a loading-unloading-recovery cycle: (a), (c) and (e) are for the strain of about 40%, while (b), (d) and (f) are for the strain of about 100%.

## A.2. One-dimensional version of the present model

A summary of the present model for one-dimensional applications is given as the following to facilitate the calibration work.

The total stretch $\lambda$ is assumed to be the same for both the entangled and non-entangled chains:

$$\lambda = \lambda_I \tag{A.1}$$

Decomposition of the stretches:

$$\lambda_I = \lambda_I^e \lambda_I^i \tag{A.2}$$

where $\lambda_I^e$ and $\lambda_I^i$ denote the elastic part and inelastic part respectively.

The logarithmic elastic strains:

$$\varepsilon_I^e = \ln \lambda_I^e \tag{A.3}$$

The Cauchy stresses:

$$\sigma = \sigma_1 + \sigma_2 + \sigma_0 \tag{A.4}$$

$$\sigma_I = E_I^e \varepsilon_I^e \tag{A.5}$$

$$\sigma_0 = \mu_0 \left(1 - \frac{\lambda^2 + 2/\lambda - 3}{I_m}\right)^{-1} \left(\lambda^2 - \frac{1}{\lambda}\right) \tag{A.6}$$

Denote $A_I$ as the principal value of $\bar{\mathbf{A}}_I$ in the uniaxial loading direction, then the GNRs can be obtained:

$$\sigma_I^a = \mu_I^a \left( A_I - \frac{1}{\sqrt{A_I}} \right) \tag{A.7}$$

The LYRs:

$$\sigma_I^i = \sigma_I - \sigma_I^a \tag{A.8}$$

The equivalent shear stresses:

$$\tau_I^i = \frac{\left|\sigma_I^i\right|}{\sqrt{3}} \tag{A.9}$$

The equivalent shear strain rates $\dot{\gamma}_I^i$ can be directly calculated according to Eqs. (61)~(67), with the mean normal pressure $p$ and the effective stretch $\lambda_1^{iEff}$ being calculated as:

$$p = -\frac{1}{3}\left(\sigma_1 + \sigma_2\right) \tag{A.10}$$

$$\lambda_1^{iEff} = \sqrt{\left(\lambda_1^{i2} + 2/\lambda_1^i\right)/3} \tag{A.11}$$

The evolution equations for the inelastic stretch:

$$\dot{\lambda}_I^i = \frac{1}{\sqrt{3}} \lambda_I^i \mathrm{sign}\left(\sigma_I^i\right) \dot{\gamma}_I^i \tag{A.12}$$

The evolution equations for $A_I$:

$$\dot{A}_I = \frac{2}{\sqrt{3}} A_I \lambda_I^i \mathrm{sign}\left(\sigma_I^i\right) \dot{\gamma}_I^i - \frac{2}{3} A_I \left( A_I - \frac{1}{\sqrt{A_I}} \right) \left( h_I \dot{\gamma}_I^i - g_I \beta_I \right) \tag{A.13}$$

where $g_I$ and the evolution of $\beta_I$ can be calculated according to Eq. (59) and Eq. (60), respectively.

In addition, the evolutions of the moduli can be directly calculated by Eqs. (68)~(74).

## A.3. Calibration procedure

After implementation of the one-dimensional model in the computer program

MATLAB, an estimate of the material parameters for the PC may be proceeded with the following steps.

1. Elasticity

As illustrated in Fig A.2(a), from the initial linear region of the stress-strain curve the Young's modulus $E_*^e$ can be obtained. $E_*^e$ equals to the sum of $E_{1*}^e$ and $E_{2*}^e$, namely,

$$E_{1*}^e + E_{2*}^e = E_*^e \tag{A.14}$$

Furthermore, a rough estimate of $E_{1*}^e$ may be achieved by the initial nonlinear stress-strain response and thus also of $E_{2*}^e$. Another elastic parameter, the Poisson's ratio $\nu$, may be chosen according to reported data in the literature (Srivastava et al., 2010).

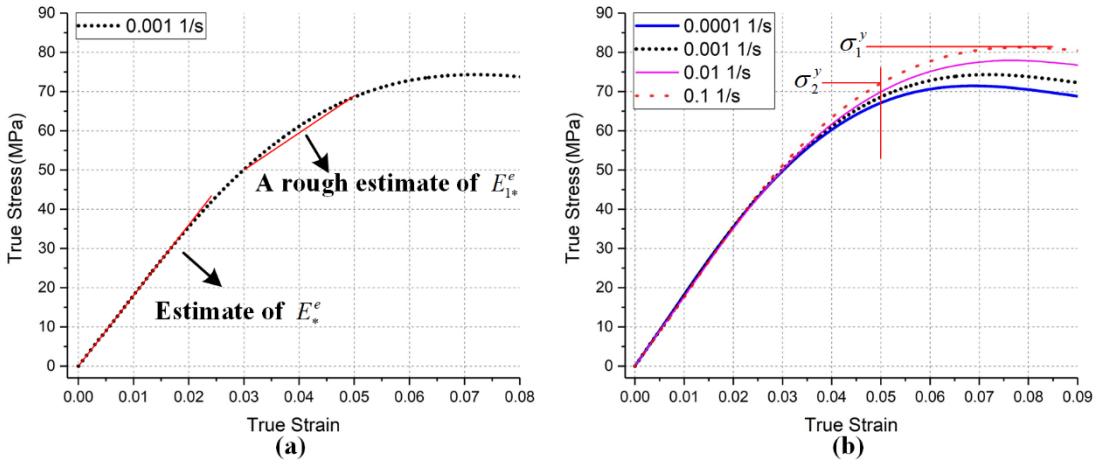


**Fig A.2** Illustration of the estimate of (a) elastic moduli and (b) yield stresses.

2. Flow laws

As illustrated by Fig A.2(b), with the yield-peak stress $\sigma_1^y$ and pre-yield stress $\sigma_2^y$ ( which may be chosen at a strain in the middle of the pre-peak hardening region) at different strain rates, a rough estimate of the material parameters in the viscoplastic flow laws can be achieved by fitting the rate-dependent yield stress with Eq. (61) and Eq. (67). Since the rate

sensitivity parameter $A$ only depends on the relative values of $\sigma_1^y$, and similarly $m$ only depends on the relative value of $\sigma_2^y$, the values of $A$ and $m$ can be fixed when adjusting the values of $\dot{\gamma}_{1*}^i$, $s_{s*}$ and $s_2$ for better fitting of the model to the yielding process. The pressure sensitivity parameter $\alpha_p$ may be chosen from the literature (Holopainen, 2013). A rough estimate of the material parameters $h_{ss}$ and $s_{seq}$ can be achieved by fitting of the model to the experimental stress-strain curve in the strain softening region. Determination of the isotropic hardening parameters $h_{sh}$ and $s_{heq}$ will be carried out later for better fitting of the model to the strain recovery data.

3. GNR

As shown by Fig A.1, the increase evolution of $\sigma_I$ determines the nonlinear pre-peak hardening region and there is a peak value for $\sigma_I$. Similar to the saturation value of the back stress in the AAS model (Ames et al., 2009), the peak value of $\sigma_I$ is mainly determined by the material parameters $\mu_{I*}^a$ and $h_I$. Thus, a rough estimate of these material parameters can be achieved by a few trials of fitting of the model to the pre-peak hardening data. The material parameters $g_{I*}$, $\chi$, and $n$ control the strain-rate dependence of the stress relaxation while the parameter $\overline{\gamma}_g^i$ controls the strain dependence of stress relaxation; they can be determined by fitting of the model with the stress relaxation and the strain recovery data.

4. RNR

The material parameters $\mu_0$ and $I_m$ can be easily obtained by fitting of the Gent model to the strain hardening data.

5. Moduli evolution

As shown by Fig A.1, $\sigma_I$ is decreased to its saturation value after the peak value. The damage parameter $\overline{\gamma}_2^a$ determines the decrease process of $\sigma_2$ and thus influences the pre-peak hardening. The damage parameter $\overline{\gamma}_1^a$ influences the decrease process of $\sigma_1$ and thus influences the strain softening. The saturation value of $\sigma_2$ is determined by the damage parameter $D_{2eq}^a$, while the saturation value of $\sigma_1$ is mainly determined by the softening parameter $s_{seq}$ and also influenced by the damage parameter $D_{1eq}^a$. The saturation value of $\sigma_I$ not only determines the flow stress but also influences the strain recovery significantly. The damage parameters $D_{1eq}^e$ and $\overline{\gamma}_1^e$ mainly affect the unloading behavior. With the above guidance, a rough estimate of these material parameters can be achieved by a few trials of fitting of the model to the loading-unloading curve.

6. Accurate estimation

Finally, more accurate estimate of the material parameters can be achieved by fitting of the model to the complete loading-unloading-recovery data as well as the stress relaxation data with the Optimization Tool provided by the computer program MATLAB. It should be noted that since some parameters control the same feature of the deformation behavior, their values may not be unique.

B. Calibrated material parameters of the BPA and AAS models

For convenient reference, the calibrated material parameters of the BPA and AAS models are denoted in the same way as the original papers.

**Table B.1**

Calibrated material parameters of the BPA model (Arruda and Boyce, 1993; Boyce et al., 1988a) for the PC glass.

| Model parameter | Unit | Value | Remark |
|---|---|---|---|
| $E$ | MPa | 1800 | Elastic |
| $\nu$ | - | 0.37 | |
| $A$ | K/MPa | 453 | Viscoplastic flow law |
| $\dot{\gamma}_0$ | $s^{-1}$ | $1.47\times10^{20}$ | |
| $h$ | MPa | 370 | Strain softening |
| $s_0$ | MPa | 81 | |
| $s_{ss}$ | MPa | 62 | |
| $\alpha_p$ | - | 0.08 | Pressure sensitivity |
| $C_R$ | MPa | 14 | Eight-chain model |
| $N$ | - | 2.38 | |

**Table B.2**

Calibrated material parameters of the AAS model (Ames et al., 2009; Srivastava et al., 2010) for the PC glass. Most of the parameters are used in the original papers, while some parameters are adjusted to fit the experimental data here.

| Model parameter | Unit | Value | Remark |
|---|---|---|---|
| $\rho$ | $kg/m^3$ | 1200 | Thermal |
| $\alpha_{gl}$ | $K^{-1}$ | $6.5\times10^{-5}$ | |
| $\alpha_r$ | $K^{-1}$ | $12\times10^{-5}$ | |
| $\nu_r$ | $s^{-1}$ | $5.2\times10^{-4}$ | |
| $\vartheta_r$ | K | 415 | |
| $n$ | K | 2.2 | |
| $\Delta$ | K | 1.6 | |
| $c_0$ | J/(kg·K) | 1630 | |
| $\kappa_0$ | Watt/(m·K) | 0.187 | |
| $\omega$ | - | 0.7 | |
| $G_{gl}$ | MPa | 650 | Elastic |
| $G_r$ | MPa | 4.0 | |

| | | | |
|---|---|---|---|
| $M_{gl}$ | MPa/K | 0.73 | |
| $M_r$ | MPa/K | 0.017 | |
| $\nu_{gl}^{poi}$ | - | 0.37 | |
| $\nu_{gl}^{poi}$ | - | 0.49 | |
| $\nu_0^{(1)}$ | $s^{-1}$ | $1.73\times10^{13}$ | Viscoplastic flow law |
| $m^{(1)}$ | - | 0.14 | |
| $V$ | $m^3$ | $1.62\times10^{-27}$ | |
| $Q_{gl}$ | J | $2.0\times10^{-29}$ | |
| $Q_r$ | J | $3.0\times10^{-20}$ | |
| $\alpha_p$ | - | 0.116 | Pressure sensitivity |
| $h_a$ | - | 80 | Yield peak (pre-peak hardening and strain softening) |
| $b$ | MPa | 5900 | |
| $g$ | - | 4.5 | |
| $z$ | - | 0.005 | |
| $r$ | - | 0.2 | |
| $s$ | - | 0.005 | |
| $h_b$ | - | 0.577 | Isotropic hardening |
| $S_{gl}$ | MPa | 55.0 | |
| $S_r$ | MPa | 0.46 | |
| $X$ | MPa/K | 2.0 | Elasto-plastic back stress |
| $\gamma$ | - | 26.0 | |
| $\mu_g$ | MPa | 3.6 | Gent model |
| $N$ | $K^{-1}$ | $13.5\times10^{-3}$ | |
| $I_m$ | - | 6.4 | |

## References


Ames, N.M., Srivastava, V., Chester, S.A., Anand, L., 2009. A thermo-mechanically coupled theory for large deformations of amorphous polymers. Part II: Applications. Int. J. Plast. 25, 1495-1539.

Anand, L., Ames, N.M., 2006. On modeling the micro-indentation response of an amorphous polymer. Int. J. Plast. 22, 1123-1170.

Anand, L., Ames, N.M., Srivastava, V., Chester, S.A., 2009. A thermo-mechanically coupled theory for large deformations of amorphous polymers. Part I: Formulation. Int. J. Plast.

25, 1474-1494.

Arruda, E.M., Boyce, M.C., 1993. Evolution of plastic anisotropy in amorphous polymers during finite straining. Int. J. Plast. 9, 697-720.

Ayoub, G., Zaïri, F., Naït-Abdelaziz, M., Gloaguen, J.M., 2010. Modelling large deformation behaviour under loading–unloading of semicrystalline polymers: Application to a high density polyethylene. Int. J. Plast. 26, 329-347.

Bending, B., Christison, K., Ricci, J., Ediger, M.D., 2014. Measurement of Segmental Mobility during Constant Strain Rate Deformation of a Poly(methyl methacrylate) Glass. Macromolecules 47, 800-806.

Bergstrom, J.S., 2015. Mechanics of solid polymers: theory and computational modeling. William Andrew.

Bouvard, J.L., Francis, D.K., Tschopp, M.A., Marin, E.B., Bammann, D.J., Horstemeyer, M.F., 2013. An internal state variable material model for predicting the time, thermomechanical, and stress state dependence of amorphous glassy polymers under large deformation. Int. J. Plast. 42, 168-193.

Boyce, M.C., Parks, D.M., Argon, A.S., 1988a. Large inelastic deformation of glassy polymers. part I: rate dependent constitutive model. Mechanics of Materials 7, 15-33.

Boyce, M.C., Parks, D.M., Argon, A.S., 1988b. Large inelastic deformation of glassy polymers. Part II: numerical simulation of hydrostatic extrusion. Mechanics of Materials 7, 35-47.

Buckley, C.P., Dooling, P.J., Harding, J., Ruiz, C., 2004. Deformation of thermosetting resins at impact rates of strain. Part 2: constitutive model with rejuvenation. Journal of the Mechanics and Physics of Solids 52, 2355-2377.

Buckley, C.P., Jones, D.C., 1995. Glass-rubber constitutive model for amorphous polymers near the glass transition. Polymer 36, 3301-3312.

Cheng, S., Wang, S.Q., 2013. Elastic yielding in cold drawn polymer glasses well below the glass transition temperature. Physical review letters 110, 065506.

Colak, O.U., 2005. Modeling deformation behavior of polymers with viscoplasticity theory based on overstress. Int. J. Plast. 21, 145-160.

Drozdov, A.D., Christiansen, J.d., 2008. Thermo-viscoelastic and viscoplastic behavior of high-density polyethylene. International Journal of Solids and Structures 45, 4274-4288.

Drozdov, A.D., Gupta, R.K., 2003. Non-linear viscoelasticity and viscoplasticity of isotactic polypropylene. International Journal of Engineering Science 41, 2335-2361.

Farrokh, B., Khan, A.S., 2010. A strain rate dependent yield criterion for isotropic polymers: Low to high rates of loading. European Journal of Mechanics - A/Solids 29, 274-282.

Garcia-Gonzalez, D., Garzon-Hernandez, S., Arias, A., 2018. A new constitutive model for polymeric matrices: Application to biomedical materials. Composites Part B: Engineering 139, 117-129.

Garcia-Gonzalez, D., Zaera, R., Arias, A., 2017. A hyperelastic-thermoviscoplastic constitutive model for semi-crystalline polymers: Application to PEEK under dynamic loading conditions. Int. J. Plast. 88, 27-52.

Gudimetla, M.R., Doghri, I., 2017. A finite strain thermodynamically-based constitutive framework coupling viscoelasticity and viscoplasticity with application to glassy polymers. Int. J. Plast. 98, 197-216.

Guo, Q., Zaïri, F., Guo, X., 2018. A thermo-viscoelastic-damage constitutive model for cyclically loaded rubbers. Part I: Model formulation and numerical examples. Int. J. Plast. 101, 106-124.

Haward, R.N., Thackray, G., 1968. The Use of a Mathematical Model to Describe Isothermal Stress-Strain Curves in Glassy Thermoplastics. Proceedings of the Royal Society of London. Series A, Mathematical and Physical Sciences 302, 453-472.

Heinz, S., Tu, J., Jackson, M., Wiggins, J., 2016. Digital image correlation analysis of strain recovery in glassy polymer network isomers. Polymer 82, 87-92.

Holopainen, S., 2013. Modeling of the mechanical behavior of amorphous glassy polymers under variable loadings and comparison with state-of-the-art model predictions. Mechanics of Materials 66, 35-58.

Holopainen, S., Barriere, T., 2018. Modeling of mechanical behavior of amorphous solids undergoing fatigue loadings, with application to polymers. Computers & Structures 199, 57-73.

Holopainen, S., Barriere, T., Cheng, G., Kouhia, R., 2017. Continuum approach for modeling fatigue in amorphous glassy polymers. Applications to the investigation of damage-ratcheting interaction in polycarbonate. Int. J. Plast. 91, 109-133.

Jena, R.K., Chester, S.A., Srivastava, V., Yue, C.Y., Anand, L., Lam, Y.C., 2011. Large-strain thermo-mechanical behavior of cyclic olefin copolymers: Application to hot embossing and thermal bonding for the fabrication of microfluidic devices. Sensors and Actuators B: Chemical 155, 93-105.

Jiang, H., Zhang, J., Yang, Z., Jiang, C., Kang, G., 2017. Modeling of competition between shear yielding and crazing in amorphous polymers' scratch. International Journal of Solids and Structures 124, 215-228.

Johnsen, J., Clausen, A.H., Grytten, F., Benallal, A., Hopperstad, O.S., 2019. A thermo-elasto-viscoplastic constitutive model for polymers. Journal of the Mechanics and Physics of Solids 124, 681-701.

Khan, A., Zhang, H., 2001. Finite deformation of a polymer: experiments and modeling. Int. J. Plast. 17, 1167-1188.

Khan, F., Yeakle, C., 2011. Experimental investigation and modeling of non-monotonic creep behavior in polymers. Int. J. Plast. 27, 512-521.

Kim, J.W., Medvedev, G.A., Caruthers, J.M., 2013. Nonlinear stress relaxation in an epoxy glass and its relationship to deformation induced mobility. Polymer 54, 3949-3960.

Klompen, E.T.J., Engels, T.A.P., Govaert, L.E., Meijer, H.E.H., 2005. Modeling of the Postyield Response of Glassy Polymers: Influence of Thermomechanical History. Macromolecules 38, 6997-7008.

Krairi, A., Doghri, I., 2014. A thermodynamically-based constitutive model for thermoplastic polymers coupling viscoelasticity, viscoplasticity and ductile damage. Int. J. Plast. 60, 163-181.

Krairi, A., Doghri, I., Schalnat, J., Robert, G., Van Paepegem, W., 2019. Thermo-mechanical coupling of a viscoelastic-viscoplastic model for thermoplastic polymers: Thermodynamical derivation and experimental assessment. Int. J. Plast. 115, 154-177.

Lee, E.W., Medvedev, G.A., Caruthers, J.M., 2010. Deformation induced evolution of mobility in PMMA. Journal of Polymer Science Part B: Polymer Physics 48, 2399-2401.

Li, W., Gazonas, G., Brown, E.N., Rae, P.J., Negahban, M., 2019. Thermomechanical model for monotonic and cyclic loading of PEEK. Mechanics of Materials 129, 113-138.

Li, X., Liu, J., Liu, Z., Tsige, M., Wang, S.-Q., 2018. Illustrating the Molecular Origin of Mechanical Stress in Ductile Deformation of Polymer Glasses. Physical review letters 120, 077801.

Liu, J., 2015. Stress Relaxation Behavior of Polymer Glasses in Both Extension and Compression. University of Akron.

Liu, J., Lin, P., Li, X., Wang, S.-Q., 2015. Nonlinear stress relaxation behavior of ductile polymer glasses from large extension and compression. Polymer 81, 129-139.

Marques, T.A., Silva, M.B., Martins, P.A.F., 2012. On the potential of single point incremental forming of sheet polymer parts. The International Journal of Advanced Manufacturing Technology 60, 75-86.

Mathiesen, D., Vogtmann, D., Dupaix, R.B., 2014. Characterization and constitutive modeling of stress-relaxation behavior of Poly(methyl methacrylate) (PMMA) across the glass transition temperature. Mechanics of Materials 71, 74-84.

Meijer, H.E.H., Govaert, L.E., 2005. Mechanical performance of polymer systems: The relation between structure and properties. Progress in Polymer Science 30, 915-938.

Miled, B., Doghri, I., Delannay, L., 2011. Coupled viscoelastic–viscoplastic modeling of homogeneous and isotropic polymers: Numerical algorithm and analytical solutions. Computer Methods in Applied Mechanics and Engineering 200, 3381-3394.

Mohagheghian, I., McShane, G.J., Stronge, W.J., 2016. Impact perforation of polymer–metal laminates: Projectile nose shape sensitivity. International Journal of Solids and Structures 88-89, 337-353.

Morelle, X., 2015. Mechanical characterization and physics-based modeling of a highly-crosslinked epoxy resin. Ph. D. thesis. Université catholique de Louvain.

Nguyen, V.D., Lani, F., Pardoen, T., Morelle, X.P., Noels, L., 2016. A large strain hyperelastic viscoelastic-viscoplastic-damage constitutive model based on a multi-mechanism non-local damage continuum for amorphous glassy polymers. International Journal of Solids and Structures 96, 192-216.

Pazmino Betancourt, B.A., Starr, F.W., Douglas, J.F., 2018. String-like collective motion in the alpha- and beta-relaxation of a coarse-grained polymer melt. The Journal of chemical physics 148, 104508.

Poulain, X., Benzerga, A.A., Goldberg, R.K., 2014. Finite-strain elasto-viscoplastic behavior of an epoxy resin: Experiments and modeling in the glassy regime. Int. J. Plast. 62, 138-161.

Qi, Z., Hu, N., Li, G., Zeng, D., Su, X., 2019. Constitutive modeling for the elastic-viscoplastic behavior of high density polyethylene under cyclic loading. Int. J. Plast.

113, 125-144.

Srivastava, V., Chester, S.A., Ames, N.M., Anand, L., 2010. A thermo-mechanically-coupled large-deformation theory for amorphous polymers in a temperature range which spans their glass transition. Int. J. Plast. 26, 1138-1182.

van Breemen, L.C.A., Klompen, E.T.J., Govaert, L.E., Meijer, H.E.H., 2011. Extending the EGP constitutive model for polymer glasses to multiple relaxation times. Journal of the Mechanics and Physics of Solids 59, 2191-2207.

Varchanis, S., Dimakopoulos, Y., Tsamopoulos, J., 2018. Evaluation of tube models for linear entangled polymers in simple and complex flows. Journal of Rheology 62, 25-47.

Wu, J.J., Buckley, C.P., 2004. Plastic deformation of glassy polystyrene: A unified model of yield and the role of chain length. Journal of Polymer Science Part B: Polymer Physics 42, 2027-2040.

Xiao, R., Nguyen, T.D., 2015. An effective temperature theory for the nonequilibrium behavior of amorphous polymers. Journal of the Mechanics and Physics of Solids 82, 62-81.

Xiao, R., Nguyen, T.D., 2016. A thermodynamic modeling approach for dynamic softening in glassy amorphous polymers. Extreme Mechanics Letters 8, 70-77.

Xiao, R., Tian, C., 2019. A constitutive model for strain hardening behavior of predeformed amorphous polymers: Incorporating dissipative dynamics of molecular orientation. Journal of the Mechanics and Physics of Solids 125, 472-487.

Yu, C., Kang, G., Chen, K., 2017a. A hygro-thermo-mechanical coupled cyclic constitutive model for polymers with considering glass transition. Int. J. Plast. 89, 29-65.

Yu, C., Kang, G., Chen, K., Lu, F., 2017b. A thermo-mechanically coupled nonlinear viscoelastic–viscoplastic cyclic constitutive model for polymeric materials. Mechanics of Materials 105, 1-15.

Yu, C., Kang, G., Lu, F., Zhu, Y., Chen, K., 2016. Viscoelastic–Viscoplastic Cyclic Deformation of Polycarbonate Polymer: Experiment and Constitutive Model. Journal of Applied Mechanics 83, 041002-041002-041014.

Zerbe, P., Schneider, B., Moosbrugger, E., Kaliske, M., 2017. A viscoelastic-viscoplastic-damage model for creep and recovery of a semicrystalline thermoplastic. International Journal of Solids and Structures 110-111, 340-350.